Prepared for submission to JHEP

Stavanger 2016/11
NORDITA-2016-121

Disfavouring Electroweak Baryogenesis and a hidden Higgs in a CP-violating Two-Higgs-Doublet Model

Anders Haarr,[a] **Anders Kvellestad,**[b] **Troels C. Petersen**[c]

[a] *Faculty of Science and Technology, University of Stavanger, 4036 Stavanger, Norway*

[b] *Nordita, KTH Royal Institute of Technology and Stockholm University, Roslagstullsbacken 23, SE-106 91 Stockholm, Sweden*

[c] *Discovery Center, Niels Bohr Institute, University of Copenhagen, Blegdamsvej 17, DK-2100 Copenhagen, Denmark*

E-mail: anders.haarr@uis.no, anders.kvellestad@nordita.org, petersen@nbi.ku.dk

Abstract: A strongly first-order electroweak phase transition is a necessary requirement for Electroweak Baryogenesis. We investigate the plausibility of obtaining a strong phase transition in a Two-Higgs-Doublet Model of type II with a minimal amount of CP violation. By performing a Bayesian fit where we constrain the scalar sector with indirect and direct measurements, we find that current data disfavours a first-order phase transition in this model. This result is mainly driven by the interplay of three effects: Constraints from the LHC Higgs data on the magnitude of the quartic couplings, the requirement of a $H^{\pm}$ heavier than around 490 GeV to avoid large contributions to $BR(b \to s\gamma)$ and the fact that a first-order phase transition requires relatively light scalar states in addition to the 125 GeV Higgs. For similar reasons we find that a "hidden-Higgs" scenario, in which the 125 GeV state is identified with the next-to-lightest scalar, is disfavoured by current data independent of any requirement on the phase transition strength.

Keywords: Electroweak Baryogenesis, Two-Higgs-Doublet Model, 2HDM, Electroweak Phase Transition, Bayesian Global Fit, Hidden Higgs

arXiv:1611.05757v1 [hep-ph] 17 Nov 2016

Contents

1 Introduction **1**

2 The model **2**
2.1 Extremization, mass matrices and parametrizations 4
2.2 Yukawa couplings 5

3 The effective potential and strength of the phase transition **5**
3.1 One-loop effective potential 6
3.2 The phase transition 7

4 Parameter scan **8**
4.1 Input parameters and prior distribution 9
4.2 Likelihood function 11
4.3 Stability condition and calculation of ξ_c 14

5 Results and discussion **15**
5.1 Interplay of a strong phase transition and experimental constraints 21
5.2 A closer look at the hidden-Higgs scenario 26

6 Conclusions **32**

A Field- and temperature-dependent masses **34**
A.1 Neutral scalars 34
A.2 Charged scalars 37
A.3 Gauge bosons 38
A.4 Fermions 38

1 Introduction

The observed baryon asymmetry of the Universe [1] has, at present, no satisfying explanation. The mechanism of Electroweak Baryogenesis, where baryon number violating processes together with a strongly first-order phase transition (FOPT) and CP violation produce the baryon asymmetry, provides a possible solution.[1] Electroweak Baryogenesis fails in the Standard Model for two reasons. Firstly, the Standard Model Higgs mass must be less than $\sim M_W$ to give a first-order phase transition [4]. Secondly, the magnitude of the CP violation in the Standard Model is not sufficient [5–8]. Models with new physics that modify the scalar sector of the SM can provide the necessary first-order phase transition

[1] For a comprehensive review see [2]. For a more recent review see [3].

[9–13], but not all of these give additional sources of CP violation, see for instance [11]. Two-Higgs-Doublet Models (2HDM) can provide both [14].

However, 2HDMs are strongly constrained by experimental data. In particular, the close agreement between the measured properties of the 125 GeV Higgs and SM predictions puts severe constraints on the theory. In 2HDMs this leads to one of two scenarios: Kinematic decoupling, where a single SM-like scalar at 125 GeV is obtained by pushing up the masses of the other scalars, or the alignment limit, where the mixing in the scalar sector is adjusted so that one of the scalars closely mimics the SM Higgs.

In the following, we consider a 2HDM of type II with a minimal amount of CP violation [15–23] and investigate how the available data from the LHC and elsewhere affect the possibility for a first-order phase transition. The question of phase transition strength in 2HDMs has been the focus of several studies [14, 24–29]. In this study we perform a Bayesian statistical fit and find that current data provides strong evidence against a first-order phase transition in the studied model.

When exploring parameter regions with a strong phase transition we find a clear preference for light scalars. This draws us to perform a dedicated analysis of the "hidden-Higgs" scenario, where the 125 GeV resonance is identified as the next-to-lightest Higgs in the model. When calculating the mass spectrum of the model to tree-level accuracy, this region of parameter space avoids significant tension with experimental data. It is however strongly disfavoured when the spectrum calculation is performed at loop level. We emphasize that this conclusion is drawn independently of the strength of the phase transition.

The remainder of the paper is organized as follows: In Sec. 2 we describe the 2HDM under consideration, while Sec. 3 is devoted to the one-loop effective potential. Here we also introduce the measure for the phase transition strength. The nuts and bolts of our Bayesian parameter scans are presented in Sec. 4, including our choice of free parameters, constraints from observables and the method used for calculating the strength of the phase transition. Our results are presented and discussed in Sec. 5. In this section, we perform five different scans. For clarity, the names and purposes of the different scans are summarized in Table 1. Lastly, our conclusions are presented in Sec. 6.

2 The model

Two-Higgs-Doublet Models differs from the SM in the scalar part of the Lagrangian:

$$\mathcal{L}_H = \sum_{a=1}^{2} [D_\mu \Phi_a]^\dagger [D^\mu \Phi_a] - V(\Phi_1, \Phi_2), \tag{2.1}$$

with the usual covariant derivative

$$D^\mu \Phi_a = [\partial^\mu - ig\sigma_j W_j^\mu - \tfrac{1}{2} i g' B^\mu] \Phi_a$$

Scan name	Purpose	Section
Prior	Illustrate the effective priors for the main and direct-search scans	4.1
Main	Scan full parameter space including all experimental data	5
Direct search	Scan full parameter space using only direct Higgs searches	5
Strong PT	Explore region with strong phase transition	5.1
Hidden Higgs: tree level	Compare to results in literature	5.2
Hidden Higgs: loop level	Extend results in literature	5.2

Table 1. Names and purposes of the parameter scans in the paper. The colors refer to the plot colors used for the different scans.

The most general renormalizable, gauge invariant scalar potential is given by [30]

$$\begin{aligned} V(\Phi_1,\Phi_2) = &-\frac{1}{2}\left[m_{11}^2\Phi_1^\dagger\Phi_1 + m_{22}^2\Phi_2^\dagger\Phi_2 + \left(m_{12}^2\Phi_1^\dagger\Phi_2 + \text{h.c.}\right)\right] \\ &+ \frac{1}{2}\lambda_1\left(\Phi_1^\dagger\Phi_1\right)^2 + \frac{1}{2}\lambda_2\left(\Phi_2^\dagger\Phi_2\right)^2 \\ &+ \lambda_3\left(\Phi_1^\dagger\Phi_1\right)\left(\Phi_2^\dagger\Phi_2\right) + \lambda_4\left(\Phi_1^\dagger\Phi_2\right)\left(\Phi_2^\dagger\Phi_1\right) \\ &+ \frac{1}{2}\left[\lambda_5\left(\Phi_1^\dagger\Phi_2\right)^2 + \text{h.c.}\right] \\ &+ \left[\left(\lambda_6\Phi_1^\dagger\Phi_1 + \lambda_7\Phi_2^\dagger\Phi_2\right)\Phi_1^\dagger\Phi_2 + \text{h.c.}\right], \end{aligned} \tag{2.2}$$

where the parameters m_{11}^2, m_{22}^2, λ_{1-4} are real, while m_{12}^2 and λ_{5-7} are complex. We constrain the model by taking $\lambda_{6,7} = 0$ in Eq. (2.2). In addition we demand that the vacuum expectation values (VEVs) of the two doublets are real in this basis. This model is sometimes referred to as the 2HDM$_5$ [18].

After setting $\lambda_{6,7} = 0$ the scalar potential respects the Z_2 symmetry $\Phi_1 \to -\Phi_1$ in the quartic terms, which helps avoid the occurrence of flavour-changing neutral currents (FCNCs). This also limits the amount of CP violation. On the other hand, the term proportional to m_{12}^2 in Eq. (2.2) breaks the Z_2 symmetry softly and allows for some CP violation. The term "soft" refers to the fact that the Z_2 symmetry is respected at small distances to all orders of the perturbative series [31].

As thoroughly described in [32, 33], the 2HDM$_5$ can exhibit CP conservation, explicit CP violation or spontaneous CP violation depending on the choice of parameter values. The conditions for the three different CP scenarios are expressed through the values of three Jarlskog-like invariants. Since we find that the data does not support a FOPT we do not investigate the values of these invariants in our analysis. Previous studies seem to suggest that the phase transition is not sensitive to a CP-violating phase [24, 26].

With the introduction of $\langle\Phi_1\rangle \equiv v\mathrm{c}_\beta$ and $\langle\Phi_2\rangle \equiv v\mathrm{s}_\beta$,[2] we parametrize the doublets as

$$\Phi_1 = \begin{pmatrix} \mathrm{G}^+\mathrm{c}_\beta - \mathrm{H}^+\mathrm{s}_\beta \\ \frac{1}{\sqrt{2}}\left[v\mathrm{c}_\beta + \eta_1 + i\left(\mathrm{G}^0\mathrm{c}_\beta - \eta_3\mathrm{s}_\beta\right)\right] \end{pmatrix} \tag{2.3}$$

$$\Phi_2 = \begin{pmatrix} \mathrm{G}^+\mathrm{s}_\beta + \mathrm{H}^+\mathrm{c}_\beta \\ \frac{1}{\sqrt{2}}\left[v\mathrm{s}_\beta + \eta_2 + i\left(\mathrm{G}^0\mathrm{s}_\beta + \eta_3\mathrm{c}_\beta\right)\right] \end{pmatrix}, \tag{2.4}$$

where the fields η_{1-3} and G^0 are real while H^+ and G^+ are complex fields. The fields G^0, G^+ and H^+ are the neutral Goldstone, charged Goldstone and charged Higgs, respectively. The η_{1-3} are not mass eigenstates, but will mix among themselves to form the mass eigenstates H_{1-3}.

2.1 Extremization, mass matrices and parametrizations

Extremizing the potential through the constraints[3]

$$\left.\frac{\partial V}{\Phi_1}\right|_{\text{vac}} = \left.\frac{\partial V}{\Phi_1^\dagger}\right|_{\text{vac}} = \left.\frac{\partial V}{\Phi_2}\right|_{\text{vac}} = \left.\frac{\partial V}{\Phi_2^\dagger}\right|_{\text{vac}} = 0 \tag{2.5}$$

yields three independent constraints, which can be used to replace the three parameters m_{11}^2, m_{22}^2 and $\mathrm{Im}(m_{12}^2)$:

$$m_{11}^2 = \left[-2\mu^2 + v^2\lambda_{345}\right]\mathrm{s}_\beta^2 + v^2\lambda_1\mathrm{c}_\beta^2 \tag{2.6}$$

$$m_{22}^2 = \left[-2\mu^2 + v^2\lambda_{345}\right]\mathrm{c}_\beta^2 + v^2\lambda_2\mathrm{s}_\beta^2 \tag{2.7}$$

$$\mathrm{Im}(m_{12}^2) = v^2\mathrm{c}_\beta\mathrm{s}_\beta\lambda_5^I, \tag{2.8}$$

where $\lambda_5^R \equiv \mathrm{Re}(\lambda_5)$, $\lambda_5^I \equiv \mathrm{Im}(\lambda_5)$, $\mu^2 \equiv \frac{\mathrm{Re}(m_{12}^2)}{2\mathrm{c}_\beta\mathrm{s}_\beta}$ and $\lambda_{345} \equiv \lambda_3 + \lambda_4 + \lambda_5^R$.

The neutral mass matrix is given by the second derivatives of V with respect to the η_i:[4]

$$\mathcal{M}^2 = \begin{pmatrix} v^2\lambda_1\mathrm{c}_\beta^2 + \mu^2\mathrm{s}_\beta^2 & (-\mu^2 + v^2\lambda_{345})\mathrm{c}_\beta\mathrm{s}_\beta & -\frac{1}{2}v^2\mathrm{s}_\beta\lambda_5^I \\ (-\mu^2 + v^2\lambda_{345})\mathrm{c}_\beta\mathrm{s}_\beta & \mu^2\mathrm{c}_\beta^2 + v^2\lambda_2\mathrm{s}_\beta^2 & -\frac{1}{2}v^2\mathrm{c}_\beta\lambda_5^I \\ -\frac{1}{2}v^2\mathrm{s}_\beta\lambda_5^I & -\frac{1}{2}v^2\mathrm{c}_\beta\lambda_5^I & \mu^2 - v^2\lambda_5^R \end{pmatrix}. \tag{2.9}$$

This mass matrix is diagonalized by a matrix R, which rotates the η_i into the mass eigenstates H_i:

$$\begin{pmatrix} \mathrm{H}_1 \\ \mathrm{H}_2 \\ \mathrm{H}_3 \end{pmatrix} = R \begin{pmatrix} \eta_1 \\ \eta_2 \\ \eta_3 \end{pmatrix}, \tag{2.10}$$

$$R\mathcal{M}^2R^T = \mathcal{M}^2_{\text{diag}} = \mathrm{diag}(m_{H_1}^2, m_{H_2}^2, m_{H_3}^2). \tag{2.11}$$

[2] $c_\beta = \cos\beta$ and $s_\beta = \sin\beta$

[3] The subscript 'vac' denotes the vacuum, where all fields are zero.

[4] The neutral mass matrix is really 4 by 4, but the neutral Goldstone contributes two lines of zeroes and an extra zero eigenvalue.

The neutral mass matrix has six independent components. Diagonalizing the charged mass matrix yields the mass of the charged Higgs

$$m_{H^\pm}^2 = \frac{1}{2}\left(2\mu^2 - v^2\left[\lambda_4 + \lambda_5^R\right]\right) \tag{2.12}$$

and a zero eigenvalue corresponding to the charged Goldstone mass. This gives six equations from the neutral sector and one from the charged sector that can be used to exchange the quartic couplings λ_i with the physical masses $m_{H_{1-3}}, m_{H^\pm}$ and three mixing angles α_{1-3}. Since the 2HDM$_5$ only has six λ_i there are different ways of substituting parameters. In [15–21] the convention is to solve for m_{H_3} and keep $\tan\beta$ as an input parameter, while [22, 23] keeps m_{H_3} as an input parameter and solves for $\tan\beta$.

Here we follow a different approach: We implement the model in the `Mathematica` package `SARAH v.4.8.6` [34] and use `SARAH` to generate a one-loop spectrum generator based on `SPheno` [35, 36]. As input parameters we take the seven Lagrangian parameters λ_{1-4}, λ_5^R, λ_5^I, $\mathrm{Re}(m_{12}^2)$ and the symmetry breaking parameter $\tan\beta$. From this input `SARAH`/`SPheno` is used to solve the loop-corrected tadpole equations to obtain the remaining Lagrangian parameters m_{11}^2, m_{22}^2 and $\mathrm{Im}(m_{12}^2)$, and calculate the scalar masses at one loop.

2.2 Yukawa couplings

The Yukawa couplings are the type-II version, where charged leptons and down-type quarks couple to Φ_1 and up-type quarks couple to Φ_2. The couplings of the neutral mass eigenstates H_j to the third-generation quarks are then given by [17]

$$H_j b\bar{b}: \quad \frac{-igm_b}{2m_W}\left(\frac{1}{\cos\beta}\left[R_{j1} - i\gamma_5 \sin\beta R_{j3}\right]\right) \tag{2.13}$$

$$H_j t\bar{t}: \quad \frac{-igm_t}{2m_W}\left(\frac{1}{\sin\beta}\left[R_{j2} - i\gamma_5 \cos\beta R_{j3}\right]\right), \tag{2.14}$$

where the R_{ji} are elements of the rotation matrix R that rotates the η_i to the physical fields H_j. The factors in the large brackets represent the change relative to the SM couplings. For the charged sector we have the couplings

$$H^+ b\bar{t}: \quad \frac{ig}{2\sqrt{2}m_W} V_{tb}\left[m_b(1+\gamma_5)\tan\beta + m_t(1-\gamma_5)\cot\beta\right] \tag{2.15}$$

$$H^- t\bar{b}: \quad \frac{ig}{2\sqrt{2}m_W} V_{tb}^*\left[m_b(1-\gamma_5)\tan\beta + m_t(1+\gamma_5)\cot\beta\right]. \tag{2.16}$$

3 The effective potential and strength of the phase transition

In this section we detail the construction of the one-loop effective potential at finite temperature. We further define notions used in our minimization procedure in Sec. 4.3 and our criterion for determining that the electroweak phase transition be first order.

3.1 One-loop effective potential

We follow [14] and utilize an $SU(2)_L \times U(1)$ gauge transformation to make the final effective potential a function of η_1, η_2, and η_3. Further, we write the effective potential in Landau gauge, in which ghosts decouple but Goldstone bosons are included in the sum over species.

The one-loop effective potential is constructed in the usual way

$$V(T) = V_{\text{tree}} + V_{\text{ct}} + V_{\text{CW}} + V_T(T), \tag{3.1}$$

where V_{tree} is the tree-level potential from Eq. (2.2), with $\lambda_{6,7} = 0$ and Φ_1, Φ_2 parametrized as in Eqs. (2.3) and (2.4). Below we describe each of the terms contributing to the effective potential in detail.

3.1.1 The Coleman-Weinberg contribution V_{CW}

When divergences have been subtracted, the one-loop contribution to the effective potential at zero temperature takes the form[5]

$$V_{\text{CW}} = \sum_i \frac{1}{64\pi^2} N_i M_i^4(\eta_j) \left[\log \frac{M_i^2(\eta_j)}{Q^2} - C_i \right], \tag{3.2}$$

where $M_i^2(\eta_j)$ are the field-dependent masses given in Appendix A, i sums over particle species and

$$\begin{aligned} N_{t,b} &= -12, \quad N_W = 6, \quad N_Z = 3, \\ N_{\text{H}_i,\text{G}^0} &= 1, \quad N_{\text{H}_\pm} = 2. \end{aligned} \tag{3.3}$$

The photon and gluons do not couple directly to the Higgs fields and so give a constant contribution to the potential as a function of η_j. They therefore play no role in locating the minimum of the potential and are ignored. In the $\overline{\text{MS}}$ scheme, C_i is 5/6 for gauge bosons and 3/2 for the rest. Q is a renormalization scale which we take to be m_t.

3.1.2 Finite-temperature contribution V_T

The one-loop correction at finite temperature is given by

$$V_T(\eta_j, T) = \sum_i \frac{T^4}{2\pi^2} N_i \int_0^\infty dx\, x^2 \log\left[1 \pm e^{-\sqrt{x^2 + \frac{M_i^2(\eta_j)}{T^2}}} \right], \tag{3.4}$$

where the N_i are defined in (3.3) and $M_i(\eta_j)$ are the field-dependent masses at zero temperature. The plus sign refers to fermions and the minus sign to bosons. This can be expanded around small $\frac{M_i}{T}$ giving [28]:

$$\text{const.} + \frac{1}{24} N_i M_i^2(\eta_j) T^2 - N_i \frac{T}{12\pi} M_i^3(\eta_j) + O(M_i^4), \qquad \text{(bosons)} \tag{3.5}$$

$$\text{const.} + \frac{1}{48} N_i M_i^2(\eta_j) T^2 + O(M_i^4), \qquad \text{(fermions)}. \tag{3.6}$$

[5] Note that finite-temperature masses enter V_{CW} after including thermal masses in Sec. 3.1.2.

Thermal corrections to the effective masses can now be included in two ways: In the "Parwani method" [27, 37] the replacement

$$M_i^2(\eta_j) \to M_i^2(\eta_j, T), \tag{3.7}$$

is made in Eqs. (3.2) and (3.4). Alternatively, the "Arnold-Espinosa method" [28, 38] exchanges

$$M_i^3(\eta_j) \to M_i^3(\eta_j, T), \tag{3.8}$$

in Eq. (3.5). In practice one adds the term

$$V_T^{\text{ring}}(\eta_j, T) = \sum_i \frac{T}{12\pi} N_i \text{Tr}\Big[M_i^3(\eta_j) - M_i^3(\eta_j, T)\Big], \tag{3.9}$$

to the potential. The cubic term from the expansion Eq. (3.5) is then effectively swapped for one that is also thermally dependent. To implement either of the methods, the thermally corrected masses, $M_i(\eta_j, T)$, must be calculated for each bosonic degree of freedom. The two methods differ by two-loop terms [27].

We follow the Parwani method. The integral in Eq. (3.4) is evaluated numerically and tabulated as a function of $\alpha_i(\eta_j, T) = M_i(\eta_j, T)^2/T^2$ for use in our numerical studies. The calculation of the thermal masses is given in Appendix A.

3.1.3 The tree-level potential V_{tree} and counterterms V_{ct}

The renormalization scheme implemented in `SARAH` and `Spheno` is the $\overline{\text{MS}}$ scheme. The specific renormalization procedure is described in [34]. In constructing $V_{\text{tree}} + V_{\text{ct}}$ we follow [39]. `Spheno` outputs both tree-level and one-loop parameters. The one-loop parameters inserted into the tree-level potential gives $V_{\text{tree}} + V_{\text{ct}}$, while the tree-level parameters go into the thermal masses. The thermal masses are used in the one-loop corrections to V described in Sections 3.1.1 and 3.1.2. We note that the calculations in `Spheno` are performed in the Feynman-'t Hooft gauge, which is the $\xi \to 1$ limit of the class of R_ξ gauges, while the effective potential is written in the Landau gauge, which is the limit $\xi \to 0$. As noted in [39], the VEVs are slightly different in these gauges. Numerically, we find this effect to be small in the physically interesting regions of parameter space.

3.2 The phase transition

At very high temperatures we have symmetry restoration, which in our parametrization means that the global minimum of the effective potential tends towards the point $(\eta_1, \eta_2, \eta_3) = (-v\cos\beta, -v\sin\beta, 0)$. We refer to the minimum that resides at this point at very high temperatures as the *symmetric minimum*.

At zero temperature the symmetry of the theory has been spontaneously broken and each of the Higgs doublets acquire a VEV, defined by the global minimum of the effective potential.[6] After `SARAH/SPheno` solves the tadpole equations, the point $(\eta_1, \eta_2, \eta_3) =$

[6] For simplicity we disregard the possibility that the broken minimum is only metastable, with a lifetime longer than the age of the universe.

$(0,0,0)$ is guaranteed to be an extremal point of the effective potential, but not necessarily a minimum. At this point the doublets satisfy $\Phi_1^\dagger\Phi_1 + \Phi_2^\dagger\Phi_2 = v^2 \approx (246\text{ GeV})^2$. For a given parameter point it is therefore necessary to check that $(\eta_1, \eta_2, \eta_3) = (0,0,0)$ is indeed the global minimum of the zero-temperature potential. In Sec. 4.3 we bundle this criterion into our stability condition. We refer to the minimum residing at the point $(\eta_1, \eta_2, \eta_3) = (0,0,0)$ when $T = 0$ as the *broken minimum*.

At intermediate temperatures the broken minimum will typically have shifted to a new position in field space. The same is true for the symmetric minimum, although the displacement in field space is generally small. We still refer to these minima as the broken and symmetric minimum at intermediate temperatures because we can track their movement in field space numerically as T varies.

The *critical temperature* T_c of the phase transition is defined as the temperature at which the global minimum shifts from the symmetric to the broken minimum, as T decreases. In a first-order phase transition, the two degenerate minima $V_{\text{br}}(T_c)$ and $V_{\text{sym}}(T_c)$ will be at different points in field space, typically with a potential barrier in between. For a second order (cross-over) transition, the broken and symmetric minimum are not degenerate until they are at the same point in field space. For such transitions, the minima melt together so that the global minimum moves continuously (smoothly) from the symmetric minimum to the broken minimum as the temperature is lowered.

The strength of the electroweak phase transition is quantified by the ratio[7]

$$\xi_c = \frac{v_c}{T_c}. \tag{3.10}$$

The parameter v_c is the VEV of the broken minimum at this temperature. In the literature a common demand for a strong enough phase transition is $\xi_c > 1$. This criterion stems from the requirement that sphalerons should be inactive in the broken phase and not equilibriate the baryon asymmetry [2]. The criterion can be relaxed to $\xi \gtrsim 0.5$ by encorporating uncertainties related to the sphaleron rate in the broken phase [44]. In Sec. 4.3 we detail our method for determining ξ_c.

4 Parameter scan

In order to determine the most probable 2HDM$_5$ parameter regions in light of current data we perform a Bayesian fit of the model. The goal of such a fit is to obtain the posterior probability density $p(\boldsymbol{\Theta}|\mathbf{D})$ for the set of model parameters $\boldsymbol{\Theta}$, given the experimental data $\mathbf{D}$. From Bayes' theorem the posterior distribution $p(\boldsymbol{\Theta}|\mathbf{D})$ is given by the prior distribution $p(\boldsymbol{\Theta}) \equiv \pi(\boldsymbol{\Theta})$ and the likelihood $p(\mathbf{D}|\boldsymbol{\Theta}) \equiv \mathcal{L}(\boldsymbol{\Theta})$,

$$p(\boldsymbol{\Theta}|\mathbf{D}) = \frac{\mathcal{L}(\boldsymbol{\Theta})\pi(\boldsymbol{\Theta})}{P(\mathbf{D})}. \tag{4.1}$$

[7] The criterion has some issues related to gauge-invariance [40]. Still, the numerical difference is believed to be small for appropriate choices of gauge, such as the Landau gauge [41, 42]. See also [43].

The denominator $P(\mathbf{D}) = \int \mathcal{L}(\mathbf{\Theta})\pi(\mathbf{\Theta})d\mathbf{\Theta}$ is the Bayesian evidence, which in our analysis only serves to normalize the posterior distribution. Our choice of prior distribution and the construction of the likelihood function will be detailed in Sections 4.1 and 4.2.

To numerically estimate $p(\mathbf{\Theta}|\mathbf{D})$ we scan the parameter space with `MultiNest v3.10` [45–47], via the Python interface `PyMultiNest` [48]. In short, `MultiNest` explores the parameter space based on a nested sampling algorithm in which a fixed number of "live points" is gradually moved towards regions of increasing likelihood [49]. This is achieved by repeatedly sampling the parameter space until a point is found with higher likelihood than the current lowest-likelihood live point. The lowest-likelihood point is then replaced by the new point in the set of live points and the process is repeated. The main purpose of `MultiNest` is to estimate the Bayesian evidence $P(\mathbf{D})$, but once the evidence has been estimated the set of current and previous live points can be re-weighted according to Bayes' theorem to produce a representative set of samples from $p(\mathbf{\Theta}|\mathbf{D})$. The performance of `MultiNest` is governed by three main settings: The number of live points (`nlive`), where a larger number ensures better coverage of the parameter space; the convergence criteria (`tol`) on `MultiNest`'s estimate of $\ln[P(\mathbf{D})]$; and an approximate sampling efficiency (`efr`) describing how strictly the sampling region should be narrowed down as the scan progresses towards higher-likelihood regions of parameter space.

The posterior predictive density for a derived quantity $f(\mathbf{\Theta})$,

$$p(f|\mathbf{D}) = \int p(f, \mathbf{\Theta}|\mathbf{D})d\mathbf{\Theta}, \tag{4.2}$$

is obtained from the posterior samples by calculating $f(\mathbf{\Theta})$ for each sample and then marginalize over the model parameters by histogramming the samples in f. In particular, we will be interested in the posterior density $p(\xi_c|\mathbf{D})$ for the phase transition strength ξ_c.

The prior and posterior distributions in a Bayesian analysis are probability densities. This has two important implications for how the results should be interpreted. First, only the shapes of the distributions are relevant. For simplicity we therefore normalize the height of the maximum probability point to unity in all plotted distributions. The total number of samples in a distribution is only a measure of the accuracy with which the probability density has been determined. Second, there is a dependence on parameter space volume. For instance, given two parameter regions with similar likelihood values, the fit will prefer the largest parameter region as measured by the integrated prior probability. In this way, a Bayesian fit automatically and consistently penalizes fine tuning in the parameters. However, this also means that if the model is defined with a large parameter space that is weakly constrained by data, this effect can dominate the posterior results.

4.1 Input parameters and prior distribution

Here we describe the input parameters and joint prior distribution used for the main scan in Sec. 5. For the other scans we specify any changes relative to the main setup when discussing the respective scan results.

As our input parameters we take

$$\lambda_1,\ \lambda_2,\ \lambda_3,\ \lambda_4,\ \lambda_5^R,\ \lambda_5^I,\ \mathrm{Re}(m_{12}^2),\ \tan\beta. \tag{4.3}$$

Priors and settings for main scan

Parameter	Range	Type	`MultiNest` setting	Value
λ_1	$[0, 4\pi]$	flat	`nlive`	4000
λ_2	$[0, 4\pi]$	flat	`tol`	0.5
λ_3	$[-4\pi, 4\pi]$	flat	`efr`	0.8
λ_4	$[-4\pi, 4\pi]$	flat	Likelihood	Included
λ_5^R	$[-4\pi, 4\pi]$	flat	Stability	Yes
λ_5^I	$[-4\pi, 4\pi]$	flat	Direct searches	Yes
$\tan\beta$	[0.1, 60]	flat	$\Delta\rho$ + B physics	Yes
$\mathrm{Re}(m_{12}^2)$	$[-1500^2, 1500^2]$ GeV^2	two-sided log	Strong PT	No
			Sampled points	Posterior
			1.6×10^7	3.3×10^4

Table 2. Prior distributions, likelihood contributions and `MultiNest` settings for the main scan. The "two-sided" log prior for $\mathrm{Re}(m_{12}^2)$ is a log prior for the magnitude $|\mathrm{Re}(m_{12}^2)|$ combined with a 50/50 prior for the sign of $\mathrm{Re}(m_{12}^2)$. Since the log prior diverges when $\mathrm{Re}(m_{12}^2) \to 0$ this prior distribution is joined by a flat prior on the range $[-10^2, 10^2]$ GeV^2.

The remaining mass-squared Lagrangian parameters m_{11}^2, m_{12}^2 and $\mathrm{Im}(m_{12}^2)$ are determined by `SPheno` by solving the loop-corrected tadpole equations.

Our joint prior distribution is based on independent priors for the input parameters. For the quartic couplings we choose flat prior distributions cut off at the perturbativity bound of $|4\pi|$. Also $\tan\beta$ is assigned a flat prior, with the range $[0.1, 60]$. $\mathrm{Re}(m_{12}^2)$ is the only dimensionful input parameter and sets the overall mass scale for the scalar sector. For this parameter we choose a log prior, i.e. a prior distribution flat in $\log[\mathrm{Re}(m_{12}^2)]$, as this is the least informative prior for a scale parameter.[8] Since $\mathrm{Re}(m_{12}^2)$ can be negative, we formulate a "two-sided" log prior that combines a log prior for the magnitude $|\mathrm{Re}(m_{12}^2)|$ over the range $[10^2, 1500^2]$ GeV^2 with a 50/50 prior on the sign. The two sides of the distribution are joined by a flat distribution on the range $[-10^2, 10^2]$ GeV^2. Our choice of individual parameter priors for the main scan is summarized in the left-hand side of Table 2.

While $\mathrm{Re}(m_{12}^2)$ sets the overall mass scale, the physical scalar masses can still deviate significantly from $\sqrt{|\mathrm{Re}(m_{12}^2)|}$ due to $\tan\beta$ and the quartic couplings. Earlier investigations of the phase transition strength in 2HDMs indicate that a not too heavy scalar mass spectrum is required for a first-order phase transition, see e.g. [14, 24, 25].[9] We have confirmed this in preliminary investigations of the high-mass region (> 1 TeV) of our model. To focus our study on parameter regions that may provide a first-order phase transition, we impose the requirement that all scalars should be lighter than 1 TeV.

[8] Most other 2HDMs scans in the literature sample the parameter space using flat distributions for the mass scale parameter or the physical masses. Looking at the results in Sec. 5, a flat prior for $\mathrm{Re}(m_{12}^2)$ would only serve to weaken the probability of a first-order phase transition in the 2HDM$_5$, thus strengthening the conclusion of our paper.

[9] However, a significant mass splitting between the heavy scalars seems to improve the possibility for a first-order phase transition.

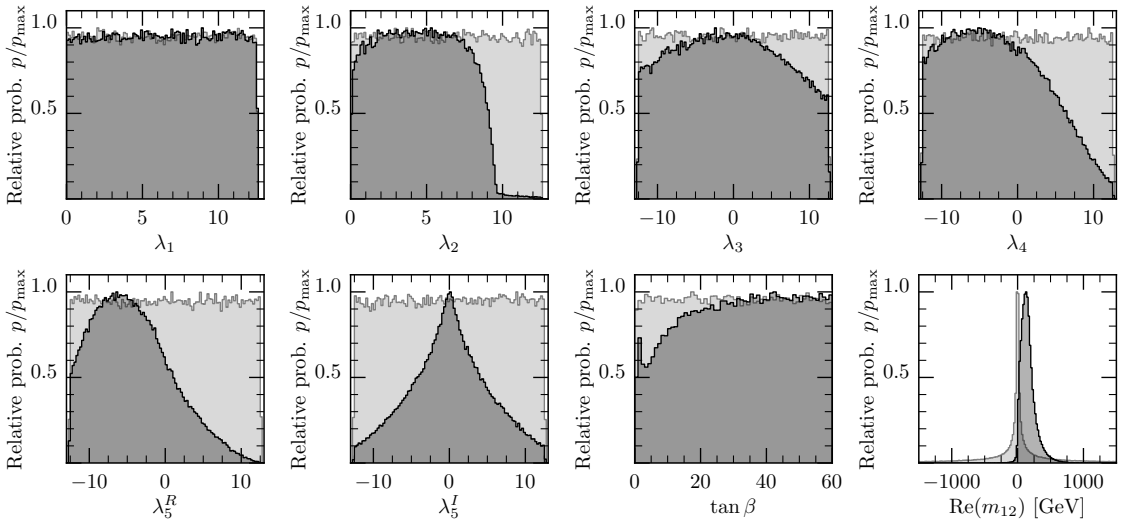

Figure 1. *Light grey:* Prior distributions for the input parameters. *Dark grey:* Effective prior distributions after requiring a physical spectrum with all scalar masses below 1 TeV. Here and in subsequent figures we use the simplified notation $\mathrm{Re}(m_{12}) \equiv \mathrm{sgn}[\mathrm{Re}(m_{12}^2)]\sqrt{|\,\mathrm{Re}(m_{12}^2)|}$.

With this additional constraint on the scalar masses the effective prior for our model is given by

$$\pi(\mathbf{\Theta}) = \prod_i H\left(1 - \frac{m_{H_i}(\mathbf{\Theta})}{\mathrm{TeV}}\right) \prod_j \pi_j(\theta_j), \tag{4.4}$$

where H is the Heaviside step function, m_{H_i} are the scalar masses and π_j are the individual parameter priors, appropriately normalized. Implicit in the constraint from H is of course also the requirement that the parameter point $\mathbf{\Theta}$ gives a physically valid spectrum. In Fig. 1 we show two sets of marginalized one-dimensional priors for the input parameters. The light grey distributions are the input priors from Tables 2 and 3, while the dark grey distributions are the effective priors resulting from from Eq. (4.4). We note that the joint requirement of obtaining a physical spectrum and having $m_{H_i} < 1$ TeV affects the parameter distributions significantly. In particular, the probability for $\mathrm{Re}(m_{12}^2) < (0\ \mathrm{GeV})^2$ or $\mathrm{Re}(m_{12}^2) > (750\ \mathrm{GeV})^2$ is greatly reduced.

4.2 Likelihood function

The likelihood function $\mathcal{L}(\mathbf{\Theta})$ is obtained by taking the predicted joint probability distribution $p(\mathbf{D}|\mathbf{\Theta})$ for the data $\mathbf{D}$ and regard this as a function of the input parameters $\mathbf{\Theta}$. When the data consists of independent observations D_i the likelihood function factorizes as

$$\mathcal{L}(\mathbf{\Theta}) = \prod_i \mathcal{L}_i(\mathbf{\Theta}). \tag{4.5}$$

We construct our likelihood function with contributions from the electroweak precision observable $\Delta\rho$; the B-physics observables ΔM_{B_s}, $BR(b \to s\gamma)$ and $BR(B_u \to \tau\nu_\tau)$; 95%

CL exclusion limits on $\sigma \times BR$ from LEP, Tevatron and LHC Higgs searches, as derived by `HiggsBounds v4.3.1` [50–54]; and a set of 85 signal rate and 4 mass measurements for the observed 125 GeV Higgs, checked using `HiggsSignals v1.4.0` [55–57].

For $\Delta\rho$, ΔM_{B_s}, $BR(b \to s\gamma)$ and $BR(B_u \to \tau\nu_\tau)$ we use likelihoods that are gaussian in the predicted observable, centred on the observed value and with a width determined by adding experimental and theoretical errors in quadrature. When only 95% CL exclusion limits are available, as for the $\sigma \times BR$ limits checked with `HiggsBounds`, we follow the approach of Ref. [66] and formulate a likelihood that is a step function at the observed limit, smeared by a 5% gaussian uncertainty. For the 125 GeV Higgs, `HiggsSignals` calculates a combined χ^2-value for the included set of mass and signal rate measurements, taking available correlations into account. We then take the likelihood contribution to be[10]

$$\mathcal{L}_{\text{HS}} = \exp\left(-\frac{\chi^2}{2}\right). \tag{4.6}$$

Below we give some further details on the individual observables.

The new contribution to $\Delta\rho$ coming from the additional scalars in the 2HDM$_5$ is calculated using Eqs. (4.10) and (4.11) in Ref. [20]. From fits to the SM [67], the allowed BSM contribution is constrained to

$$\Delta\rho = (4.0 \pm 2.4) \times 10^{-4}. \tag{4.7}$$

Phenomenologically, the effect of this constraint is to force the mass splitting between $H^\pm$ and either H_2 or H_3 to be small, typically within a few tens of GeV.

The B_s-$\bar{B}_s$ mixing observable ΔM_{B_s} is sensitive to box diagrams involving $H^\pm$ and quarks, with the top quark contribution generally dominating. We use the theory calculation provided by the `SARAH`-generated version of `SPheno`. To this calculation we assign a conservative 20% theory error to account for uncertainties in phenomenological parameters in the hadronic matrix element, and the fact that the calculation only includes the top quark contributions. For the observed value we take the LHCb and CDF average from Ref. [68],

$$\Delta M_{B_s} = 17.757 \pm 0.021 \text{ ps}^{-1}. \tag{4.8}$$

Due to the dependence on the top Yukawa coupling, the main effect of this observable is to disfavour very low values of $\tan\beta$.

The decay $B_u \to \tau\nu$ can be mediated by a charged Higgs at tree level. In the type-II 2HDM this alters the predicted $BR(B_u \to \tau\nu)$ by a factor $[1 - (m_B^2/m_{H^\pm}^2)\tan^2\beta]^2$ relative to the SM prediction [69, 70]. Hence, for small $m_{H^\pm}$ and large $\tan\beta$, the predicted branching ratio can deviate significantly from the SM prediction. We calculate the predicted

[10] This likelihood contribution is missing the usual gaussian normalization factor, $(\sqrt{2\pi}\sigma)^{-1}$. A constant factor in a likelihood does not affect the posterior distribution as it cancels between the likelihood and evidence in Eq. (4.1). With a parameter-dependent theory error, $\sigma = \sigma(\boldsymbol{\Theta})$, this is no longer true. However, when theory errors are estimated to be a fraction of the theory prediction and the data is strongly constraining, as is the case for the 125 GeV Higgs, this effect remains small across the parameter regions that give a reasonable fit to the data.

branching ratio using `SuperIso v3.4` [71, 72] and take the experimental average

$$BR(B_u \to \tau\nu) = (1.14 \pm 0.22) \times 10^{-4} \tag{4.9}$$

as the observed value [68].

At leading order in the SM, the FCNC process $b \to s\gamma$ proceeds through a W-quark loop. In the 2HDM there are additional contributions from loops where the W is replaced by a charged Higgs. We calculate the theory prediction with `SuperIso` and use the average from Ref. [68] as the observed value,

$$BR(b \to s\gamma) = (3.43 \pm 0.22) \times 10^{-4}, \tag{4.10}$$

with statistical and systematic uncertainties added in quadrature. We find that, at large $\tan\beta$, $m_H^{\pm} > 493$ GeV is required to avoid $> 2\sigma$ tension with the observed value, in agreement with Refs. [73, 74]. For low $\tan\beta$ the constraint on $m_{H^{\pm}}$ gets even stronger.

We use the effective coupling approach in `HiggsBounds` to test the extended Higgs sector of the 2HDM against exclusion limits from Higgs searches at LEP, Tevatron and LHC. Here we give a brief summary of the method: First, for each Higgs boson H_i the relevant theory prediction, typically $(\sigma \times BR)^{\rm th}_{H_i}$, is calculated for each search, using masses, decay rates and effective couplings provided by `SPheno`. This is then compared to the *expected* limits for the different searches, in order to determine which search is expected to give the strongest constraint. Finally, for the search channel found to have the strongest expected sensitivity, the theory prediction is compared to the observed limit through the ratio

$$R_i = \frac{(\sigma \times BR)^{\rm th}_{H_i}}{(\sigma \times BR)^{\rm lim}_{H_i}}, \tag{4.11}$$

so that $R_i > 1$ signifies exclusion at the 95% CL. The overall result is then taken to be

$$R = \max_i R_i, \tag{4.12}$$

which we use to formulate our smeared upper-limit likelihood at $R = 1$. For further details on the methodology of `HiggsBounds` and which searches are included, we refer the reader to Refs. [50–54].

To test the model against the measurements of the observed 125 GeV signal, we run `HiggsSignals` in the "peak-centered" mode. In this mode, `HiggsSignals` calculates a χ^2 for the hypothesis that a signal observed at a specific mass is explained by the model. The total χ^2 is a sum of contributions from both signal rate and mass measurements. For the signal rates, the basis for comparison with experimental results is the signal rate modifier,

$$\mu = \sum_i \omega_i \frac{(\sigma \times BR)^{\rm th}_i}{(\sigma \times BR)^{\rm SM}_i}. \tag{4.13}$$

Here i denotes the specific channels considered in the experimental analysis and the ω_i are the SM channel weights, defined as

$$\omega_i = \frac{\epsilon_i (\sigma \times BR)^{\rm SM}_i}{\sum_j \epsilon_j (\sigma \times BR)^{\rm SM}_j}, \tag{4.14}$$

where ϵ_i is the relative experimental efficiency for channel i. We run `HiggsSignals` with an assigned 1% theory error on the predicted Higgs boson masses. Further details on the χ^2 calculation in `HiggsSignals` can be found in Refs. [55–57].

We use the most up-to-date Higgs data sets included in `HiggsBounds v4.3.1` and `HiggsSignals v1.4.0`. For the 125 GeV Higgs data in `HiggsSignals` this includes analyses published prior to July 2015,[11] while for `HiggsBounds` analyses published before October 2015 are included. No Higgs searches at 13 TeV are included in our analysis. As we will see, the level of agreement with SM predictions seen in the 7/8 TeV data is already enough to strongly favor the regions of 2HDM$_5$ parameter space with SM-like predictions. Since the ATLAS+CMS Higgs combination [58] and 13 TeV Higgs data so far [59–62] show no evidence of deviations from the SM, we expect that including this data would only strengthen the conclusions of our analysis.

In the next subsection we detail our check of positivity and stability for the zero-temperature effective potential. Parameter points that fail this check are assigned zero likelihood. We do not impose the commonly used constraint on tree-level perturbative unitarity [63], which places upper bounds on combinations of the quartic couplings.[12] However, we have investigated the expected impact by checking how the posterior distributions from our scans change when discarding samples that fail this constraint. Relative to the results presented in Sec. 5, the most important difference is that λ_1 is constrained to $\lambda_1 < 8.4$. For the main and direct-search scans in Sec. 5 the only other difference is a slightly increased preference for lower values of $|\lambda_3|$, $|\lambda_4|$ and $|\lambda_5^R|$, as well as for lower values of $\tan\beta$, due to a correlation with λ_1. This has no impact on the conclusions we draw from these scans. For the strong-PT scan presented in Sec. 5.1 the perturbative unitarity constraint has virtually no impact on the posterior distributions. In the case of the hidden-Higgs scans the impact is more significant and we give a dedicated discussion of this in Sec. 5.2. We will find that enforcing tree-level perturbative unitarity strengthens the conclusion that the hidden-Higgs scenario is disfavoured by current data.

4.3 Stability condition and calculation of ξ_c

Before calculating the phase transition strength ξ_c for a given parameter point, we need to establish the positivity of $V(T=0)$ and the stability of the broken minimum. Using `MINUIT2` [75] we first minimize $V(T=0)$ in the vicinity of $(\eta_1, \eta_2, \eta_3) = (0,0,0)$ to establish that the vacuum corresponds to a minimum of the effective potential. Next, we minimize $V(T=0)$ multiple times, starting from different points at large field values. If a minimum deeper than the SM minimum is found, or if the minimization algorithm tends towards too large field values, $|\eta_i| > 20 m_t$, we regard the potential as unstable. Similarly, we also check that for very high temperatures, the only minimum of $V(T)$ is the symmetric minimum, $V_{\rm sym}$, in $(\eta_1, \eta_2, \eta_3) = (-v\cos\beta, -v\sin\beta, 0)$. In what follows we will refer to these constraints collectively as the "stability condition".

[11] While this does not include the final combination of ATLAS and CMS Higgs measurements at 7/8 TeV [58], almost all the individual measurements contributing to that combination are included.

[12] Perturbative unitarity bounds have recently been computed at the one-loop level for CP-conserving 2HDMs [64]. The impact of this on a Bayesian global fit is studied in [65].

The complete stability check requires repeated numerical minimization of the effective potential. Due to this computational expense it is impractical to include this check directly in the scan likelihood for a large scan. A workaround is then to run the scan with the likelihood constructed from the observables described in the previous section, and afterwards perform the stability check on all points in the resulting posterior distribution. By discarding posterior points that fail the stability condition we effectively re-weight the posterior to incorporate the stability condition. As long as the scan sample the posterior distribution with high enough accuracy, this re-weighting is equivalent to including the stability check directly in the scan likelihood. This is the approach we use for the main and direct-search scans in Sec. 5, which are the largest scans in our study. For the medium-sized hidden-Higgs scans in Sec. 5.2 the check that the vacuum is a minimum is included in the scan likelihood, but the complete stability check is again only done on the resulting posterior samples. Finally, for the smaller strong-PT scan in Sec. 5.1 the complete stability check is included directly in the scan likelihood.

For points that pass the above checks we can go on to calculate ξ_c. We need to determine the critical temperature T_c and the field space distance v_c between $V_{\rm br}(T_c)$ and $V_{\rm sym}(T_c)$. A simple algorithm is used to estimate T_c: Starting from $T = 0$ GeV, we increase the temperature in small steps ΔT, for each step tracking the position of the broken minimum by minimizing the potential with `MINUIT2`. When a temperature is reached for which $V_{\rm sym}(T) < V_{\rm br}(T)$, the step size ΔT is reduced and the algorithm is repeated, starting from the previous temperature, for which $V_{\rm sym}(T) > V_{\rm br}(T)$. We use the step sizes $\Delta T = 20$, 2 and 0.2 GeV. As pointed out in [14], the symmetric minimum can develop a non-zero VEV at lower temperatures. To take this into account we track the position of $V_{\rm sym}$ by minimizing the potential in the region around $(\eta_1, \eta_2, \eta_3) = (-v\cos\beta, -v\sin\beta, 0)$ each time ΔT is reduced. We note that there is a possibility of having several minima at intermediate temperatures, which may alternate between being the global minimum. Since we track the global minimum from its position at zero temperature we might miss multi-step transitions occurring at intermediate temperatures.

5 Results and discussion

For the result of our main scan we combine the posterior samples from four identical `MultiNest` scans. The scan likelihood function include all the observables discussed in Sec. 4.2. The choice of priors, `MultiNest` settings and included likelihood contributions are summarized in Table 2. In total, the scans visited around 1.6×10^7 parameter points, producing a posterior distribution of 6×10^4 points. After discarding posterior samples that fail the stability condition, we end up with a posterior distribution of 3.3×10^4 samples.

To illustrate the impact of the direct Higgs searches and measurements alone we also perform a "direct-search scan" where we only include the likelihood contributions calculated with `HiggsBounds` and `HiggsSignals`, leaving out the stability condition, $\Delta\rho$ and the B-physics observables. In this case the result consists of the combined posterior samples from two identical scans, with the scan details summarized in Table 3.

Priors and settings for direct-search scan

Parameter	Range	Type	`MultiNest` setting	Value
λ_1	$[0, 4\pi]$	flat	`nlive`	4000
λ_2	$[0, 4\pi]$	flat	`tol`	0.5
λ_3	$[-4\pi, 4\pi]$	flat	`efr`	0.8
λ_4	$[-4\pi, 4\pi]$	flat	Likelihood	Included
λ_5^R	$[-4\pi, 4\pi]$	flat	Stability	No
λ_5^I	$[-4\pi, 4\pi]$	flat	Direct searches	Yes
$\tan\beta$	[0.1, 60]	flat	$\Delta\rho$ + B physics	No
$\mathrm{Re}(m_{12}^2)$	$[-1500^2, 1500^2]$ GeV^2	two-sided log	Strong PT	No
			Sampled points	Posterior
			5.5×10^6	2.4×10^4

Table 3. Prior distributions, likelihood contributions and `MultiNest` settings for the direct-search scan. Compared to the main scan, only direct Higgs search and measurement results are included as constraints, while $\Delta\rho$ + B physics and stability complience has not been considered.

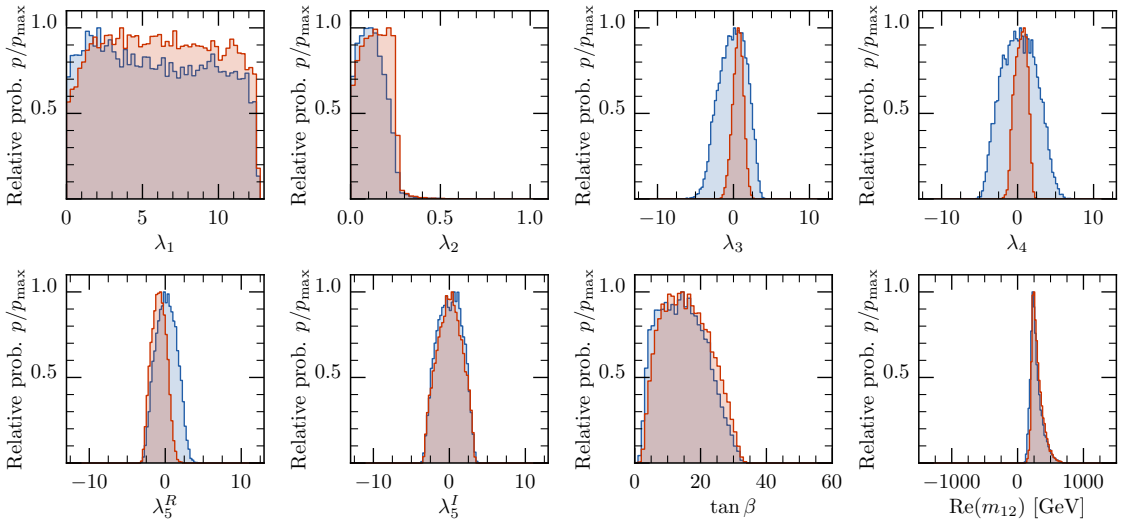

Figure 2. Marginalized posterior distributions for the input parameters. *Red:* The result of the main scan with all likelihood contributions included. *Blue:* The result of the direct-search scan, which includes likelihood contributions from direct Higgs searches and measurements. Note that the plotted range for λ_2 is [0, 1], in contrast to Fig. 1, where it is [0, 13].

In Fig.2 we show the marginalized posterior distributions for the input parameters. The result of the direct-search scan is shown in blue, while the main scan results are shown in red. Comparing first the posteriors from the direct-search scan in blue with the effective priors in dark grey from Fig.1, we see that the direct-search observables constrain the probable ranges of all quartic couplings except λ_1. Most notably, there is a clear preference for $\lambda_2 < 0.3$. This is due to the Higgs mass measurement and the fact that in the alignment limit $m_{H_1}^2$ is at tree level dominated by the term $v^2\lambda_2 s_\beta^2$, appearing in element $(\mathcal{M}^2)_{22}$ in Eq. (2.9). For $\tan\beta \gg 1$ the observed value $m_{H_1} \approx 125$ GeV then

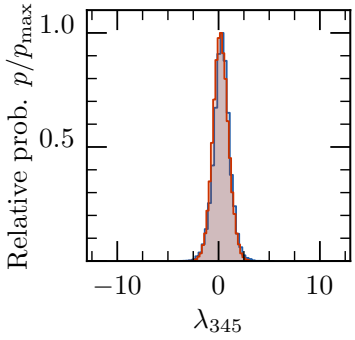

Figure 3. Marginalized posterior distributions for $\lambda_{345} \equiv \lambda_3 + \lambda_4 + \lambda_5^R$ from the main scan (red) and the direct-search scan (blue).

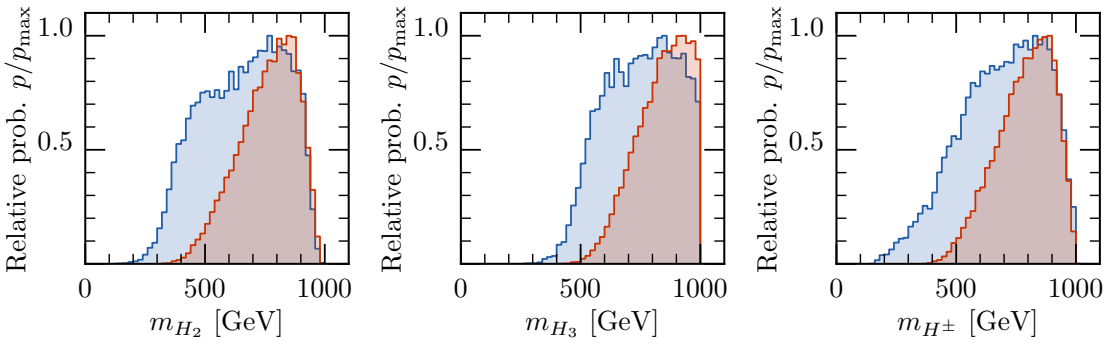

Figure 4. Marginalized posterior distributions for the heavy scalar masses. *Red:* The result of the main scan with all likelihood contributions included. *Blue:* The result of the direct-search scan, which includes likelihood contributions from direct Higgs searches and measurements.

implies $\lambda_2 \approx (125\text{ GeV})^2/(246\text{ GeV})^2 \approx 0.26$. Except for λ_1, the least constrained quartic couplings are λ_3 and λ_4. At tree level these couplings only appear in the neutral-scalar mass matrix through the combination $\lambda_{345} \equiv \lambda_3 + \lambda_4 + \lambda_5^R$, see Eq. (2.9). As a consequence, λ_{345} is more strongly constrained by the Higgs data than the individual couplings. The posterior distribution for λ_{345} is shown in Fig. 3, where we see that $|\lambda_{345}| < 2.5$ is favoured.

Probable $\tan\beta$ values are limited to the range $(1.5, 33)$. This is mainly due to the type-II Yukawa couplings. At very low $\tan\beta$ we have enhanced rates for processes depending on the ttH_i vertex, e.g. gluon fusion production, while at large $\tan\beta$ the vertices bbH_i and $\tau\tau H_i$ become important. Finally, we see that the Higgs searches and measurements are most easily fit when the free mass scale parameter $\mathrm{Re}(m_{12}^2)$ is greater than about $(100\text{ GeV})^2$.

Moving on to the posterior distributions from the main scan in red, we see that the preferred ranges for λ_3, λ_4 and λ_5^R are further narrowed and low values of $\tan\beta$ and $\mathrm{Re}(m_{12}^2)$ are more strongly disfavoured. The most important additional effect come from the observables $\Delta\rho$ and $BR(b \to s\gamma)$. While $\Delta\rho$ limits the mass difference between $m_{H^\pm}$ and m_{H_2}, $BR(b \to s\gamma)$ disfavours low values of $m_{H^\pm}$. As a consequence, the preferred ranges for the scalar masses are pushed above ~ 400 GeV. This is illustrated in Figs. 4

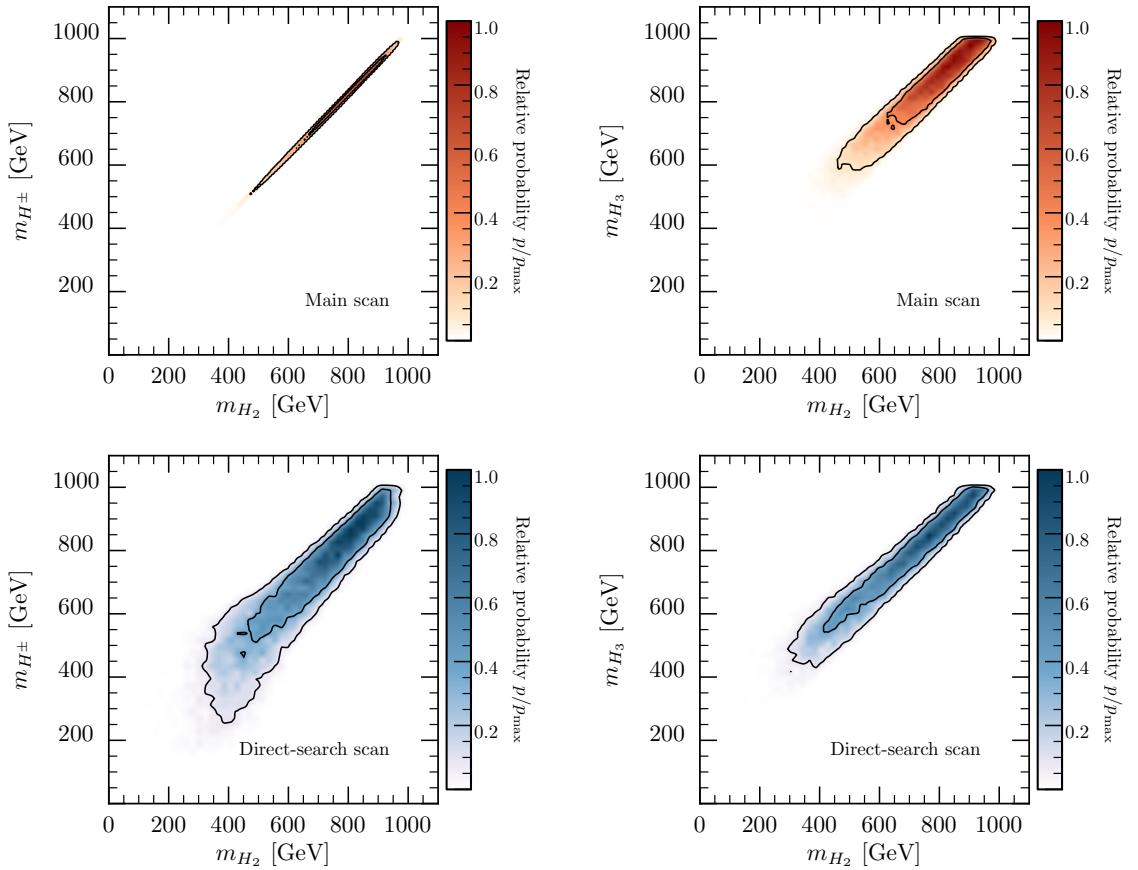

Figure 5. Two-dimensional marginalized posterior distributions in the planes of m_{H_2} vs. $m_{H^\pm}$ (left) and m_{H_2} vs. m_{H_3} (right). *Top row:* Results from the main scan with all likelihood contributions included. The contours depict the 68% and 95% credible regions. *Bottom row:* Results from the direct-search scan, which includes likelihood contributions from direct Higgs searches and measurements.

and 5, which show one- and two-dimensional posterior distributions for the heavy scalars, for both the direct-search scan and the main scan. The inner and outer contours in Fig. 5 are the 68% and 95% Bayesian credible regions, respectively. We note that the constraints coming from the direct Higgs searches and measurements limit the preferred $m_{H_3} - m_{H_2}$ mass difference to $m_{H_3} - m_{H_2} \lesssim 200$ GeV, as can be seen in the bottom right plot of Fig. 5.

The preferred parameter region exhibits strong SM alignment, with the couplings of $H_{2,3}$ to gauge boson pairs vanishing while H_1 adopts SM-like couplings. To illustrate this we plot the posterior distributions of the squared couplings of H_1 to gauge boson pairs normalized to the corresponding SM couplings,

$$\hat{g}^2_{H_1 ii} \equiv \left(\frac{g_{H_1 ii}}{g_{H_{\rm SM} ii}} \right)^2, \quad i = Z, W, \gamma, g, \tag{5.1}$$

where the couplings to gluons and photons are understood as the effective loop-induced

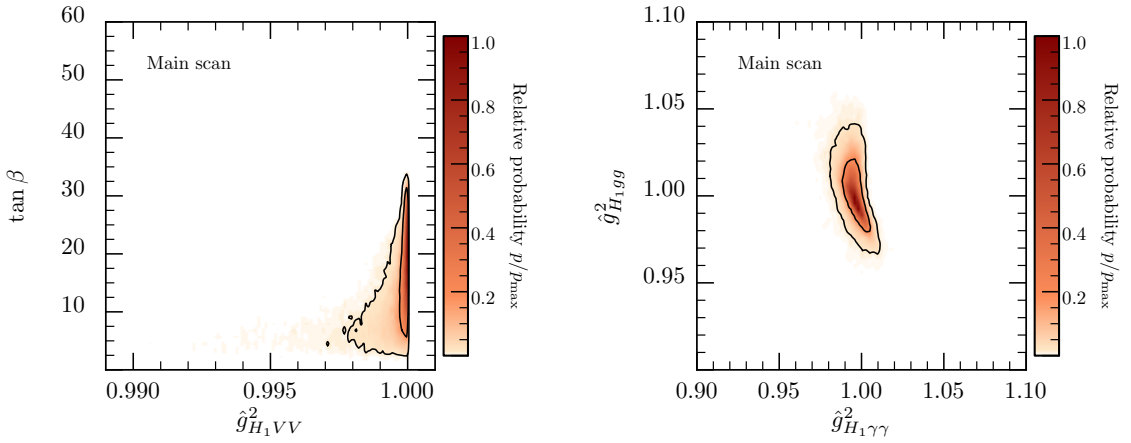

Figure 6. Two-dimensional marginalized posterior distributions in the planes of $\hat{g}^2_{H_1VV}$ vs. $\tan\beta$ (left) and $\hat{g}^2_{H_1\gamma\gamma}$ vs. $\hat{g}^2_{H_1gg}$ (right). The contours show the 68% and 95% credible regions.

couplings. The left-hand plot of Fig. 6 shows the marginalized posterior in the plane of $\hat{g}^2_{H_1VV}$ ($V = Z, W$) and $\tan\beta$. The 95% credible region prefers $\hat{g}^2_{H_1VV}$ values within a few permille of the SM value. The right-hand plot of Fig. 6 depicts the marginalized posterior in the plane of the two loop-induced couplings $\hat{g}^2_{H_1\gamma\gamma}$ and $\hat{g}^2_{H_1gg}$. In this case, the fit prefers deviations from alignment of no more than a few percent.

The high degree of SM alignment preferred by the fit is in part driven by the volume effect discussed in Sec. 4. Even when all scalars are kept below 1 TeV there is a large parameter volume available that produces a highly SM-like Higgs at 125 GeV and avoids any tension with the other observables.[13] Thus, when considering the "full" 2HDM$_5$ parameter space as scanned here, the most probable scenario for fitting all the experimental data is one in which the properties of H_1 agree closely with SM predictions. One manifestation of the strong SM alignment is the absence of a second "branch" extending towards smaller $\hat{g}^2_{H_1VV}$ values in the left-hand plot of Fig. 6. As shown for the CP-conserving type-II 2HDM in Refs. [76, 77], the Higgs signal rates predicted by that parameter region only agree with SM predictions to within $\sim 10\%$.

We now go on to investigate the probability for having a first-order phase transition. First we note that given our choice of prior distribution for the input parameters, the *prior* probability for a strong phase transition is already quite small. This can be seen in the grey distribution in Fig. 7, which shows the prior predictive distribution for ξ_c, given that the stability condition (S) is satisfied, $p(\xi_c|S)$. The distribution is based on around 1.4×10^5 samples satisfying the stability condition, out of a total of 2×10^5 prior samples. The $\sim 1\%$ upper tail of the distribution corresponds to $\xi_c > 0.57$.

Now the interesting question is whether fitting the model to the observed data has made large ξ_c values a more probable prediction. The answer is contained in the posterior predictive distribution, $p(\xi_c|\mathbf{D}, S)$, shown as the red distribution in Fig. 7. This distribution is based on the 3.3×10^4 posterior samples satisfying the stability condition. Despite the

[13] This volume effect would be even more pronounced had we used a flat prior for $\mathrm{Re}(m^2_{12})$.

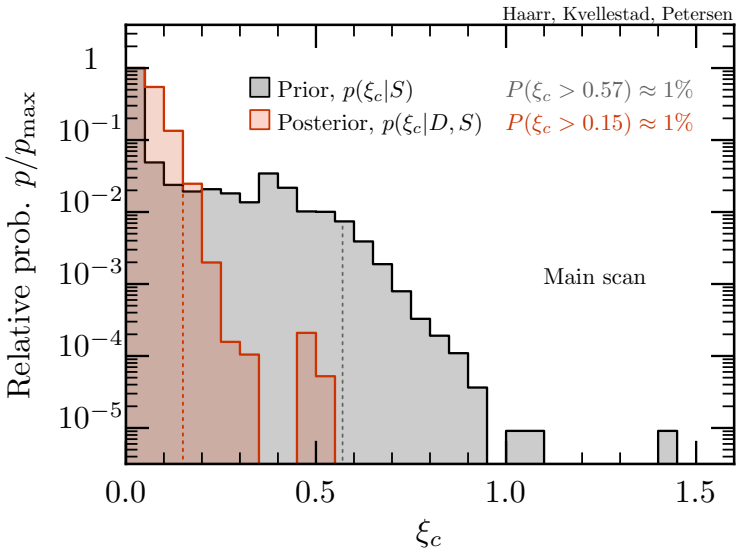

Figure 7. Comparison of the prior predictive (grey) and posterior predictive (red) distributions for the phase transition strength ξ_c, given that the stability condition S is satisfied. The dotted lines at $\xi_c = 0.15$ and $\xi_c = 0.57$ delimit the 1% upper tails of the distributions. There are no posterior samples with $\xi_c > 0.6$, indicating that a FOPT is highly unlikely.

more limited statistics, we clearly see that the posterior distribution for ξ_c drops off much more quickly compared to the prior distribution. In particular, the 1% upper tail of the distribution starts already at $\xi_c > 0.15$ and there are no posterior samples with $\xi_c > 0.6$. We note that the few posterior samples with $\xi_c \approx 0.5$ have $\tan\beta \in (2, 5)$ and scalar masses in the ranges $m_{H_2} \in (550, 650)$ GeV, $m_{H_3} \in (630, 730)$ GeV and $m_{H^\pm} \in (580, 700)$ GeV, which are all towards the lower ends of the respective posterior distributions.

As an alternative way of illustrating the impact of the data, we can construct the ratio of the posterior and prior probabilities for $\xi_c > r$,

$$\frac{P(\xi_c > r|\mathbf{D}, S)}{P(\xi_c > r|S)} = \frac{P(\mathbf{D}|\xi_c > r, S)}{P(\mathbf{D}|S)}, \tag{5.2}$$

where the equality follows from rewriting $P(\xi_c > r|\mathbf{D}, S)$ using Bayes' theorem. Thus, the ratio describes how probable the observed data is across the region of parameter space satisfying both stability and $\xi_c > r$, compared to the wider region satisfying only the stability constraint. In Fig. 8 we plot this ratio as a function of r from 0 to 0.5. We see that when constraining the model to the region $\xi_c > 0.25$, the relative probability for the observed data $\mathbf{D}$ is reduced by two orders of magnitude. The right-hand side in Eq. (5.2) can also be interpreted as the reciprocal Bayes factor for the two competing hypotheses $H_a : S$ and $H_b : S, \xi_c > r$. According to Jeffreys scale [78], the data constitutes "very strong" evidence in favor of H_a for $\xi_c > 0.2$. This is indicated by the shaded bands in Fig. 8.

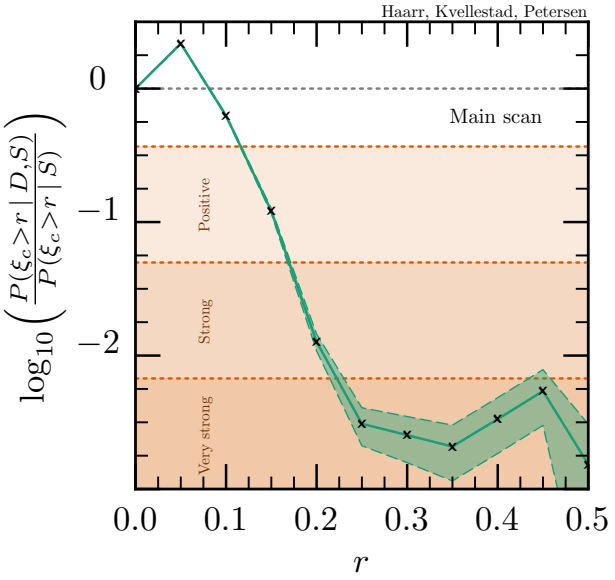

Figure 8. The ratio of the posterior and prior probabilities for a phase transition strength $\xi_c > r$, given that the stability condition (S) for the effective potential is satisfied. The green band is the estimated 1σ uncertainty due to limited statistics. The plotted ratio corresponds to the reciprocal Bayes factor for the two hypotheses $H_a : S$ and $H_b : S$, $\xi_c > r$. The orange lines depict the Jeffreys scale limiting values for "positive", "strong" and "very strong" evidence in favour of H_a [78].

Even though we divide out the prior probability for $\xi_c > r$ in Eq. (5.2), the result in Fig. 8 still has a dependence on the prior for the input parameters, as any Bayesian analysis will. This can be seen explicitly by expressing the right-hand side of Eq. (5.2) as

$$\frac{P(\mathbf{D}|H_b)}{P(\mathbf{D}|H_a)} = \frac{\int p(\mathbf{D}|\mathbf{\Theta}, H_b)p(\mathbf{\Theta}|H_b)d\mathbf{\Theta}}{\int p(\mathbf{D}|\mathbf{\Theta}, H_a)p(\mathbf{\Theta}|H_a)d\mathbf{\Theta}}. \tag{5.3}$$

The factors $p(\mathbf{\Theta}|H_a)$ and $p(\mathbf{\Theta}|H_b)$ are nothing but the input prior distributions for the parameters $\mathbf{\Theta}$ under the additional constraint of H_a and H_b, respectively. In the limit where the chosen input prior $p(\mathbf{\Theta})$ reflects certainty in hypothesis H_b, i.e. only points satisfying stability and $\xi_c > r$ are assigned a non-zero prior probability, we would have $P(H_b) = 1$, and since $P(H_a|H_b) = 1$ the ratio in Eq. (5.3) would be unity for any data $\mathbf{D}$. Thus, the value in our result lies in the fact that we use a fairly non-informative prior distribution and then explore in what direction the data take us.

5.1 Interplay of a strong phase transition and experimental constraints

In the previous section we found that the 2HDM_5 does not predict a first-order phase transition when fitted to the experimental data. However, we also saw that the sheer volume of the weakly constrained parameter regions had an important impact on the fit. One might therefore worry that our conclusion regarding the probability of a FOPT comes with a strong prior dependence. To check our conclusion we therefore perform a new parameter scan with `MultiNest`. The likelihood function is the same as in the main scan,

Priors and settings for the strong-PT scan

Parameter	Range	Type	`MultiNest` setting	Value
λ_1	$[0, 4\pi]$	flat	`nlive`	500
λ_2	$[0, 1]$	flat	`tol`	0.5
λ_3	$[-4\pi, 4\pi]$	flat	`efr`	0.8
λ_4	$[-4\pi, 4\pi]$	flat	Likelihood	Included
λ_{345}	$[-5, 5]$	flat	Stability	Yes
λ_5^I	$[-4\pi, 4\pi]$	flat	Direct searches	Yes
$\tan\beta$	$[0.1, 60]$	flat	$\Delta\rho$ + B physics	Yes
$\mathrm{Re}(m_{12}^2)$	$[-1500^2, 1500^2]$ GeV^2	two-sided log	Strong PT	Yes
			Sampled points	Posterior
			5.2×10^6	4.7×10^3

Table 4. Prior distributions, likelihood contributions and `MultiNest` settings for the strong-PT scan.

except that we now also include the requirement $\xi_c > 1$ as a 95% CL lower limit. Thus, the scan is forced to search for parameter regions with a strong phase transition while at the same time staying in as close agreement with other constraints as possible. We refer to this scan as the "strong-PT scan".

Due to the computational expense of calculating ξ_c for every point in the scan, the scope of the scan must be restricted: First, in light of the preference for small λ_{345} in the main scan, we now take λ_{345} as an input parameter with a flat prior on $[-5, 5]$. λ_5^R is then determined from $\lambda_5^R = \lambda_{345} - \lambda_3 - \lambda_4$, with the constraint that $|\lambda_5^R| < 4\pi$. Further, we restrict the λ_2 prior to the range $[0, 1]$. Our choice of priors, `MultiNest` settings and likelihood contributions are summarized in Table 4. We here run two identical `MultiNest` scans with only 500 live points (`nlive = 500`) and combine the posterior samples. It should be noted that such a low number of live points is not enough to guarantee a complete exploration of a large parameter space. However, here we are mainly interested in using the scan to further understand and cross-check the results of the larger scan in the previous section.

In Fig. 9 we show the obtained posterior distributions for the parameters (purple). As a result of demanding a strong phase transition, all input parameters except for λ_1 and $\tan\beta$ are rather tightly constrained. The model has for the most part been pushed into the hidden-Higgs scenario, where the next-to-lightest Higgs, H_2, is identified with the 125 GeV resonance. The "standard scenario" with H_1 as the 125 GeV Higgs only accounts for around 1% of the posterior probability. In Fig. 9 the contribution from the standard scenario to the overall posterior is shown as orange histograms, scaled up for visibility.

Before discusssing why the preferred parameter region in this scan is in tension with observations, we note a couple of characteristics that agree well with the findings of previous studies: Firstly, allowing for a non-zero CP-violating phase does not seem to be important for having a strong phase transition [24, 26]. This is seen in the preference for small λ_5^I. When $\lambda_5^I = 0$ the Jarlskog-like CP-invariants vanish and we have no CP violation and

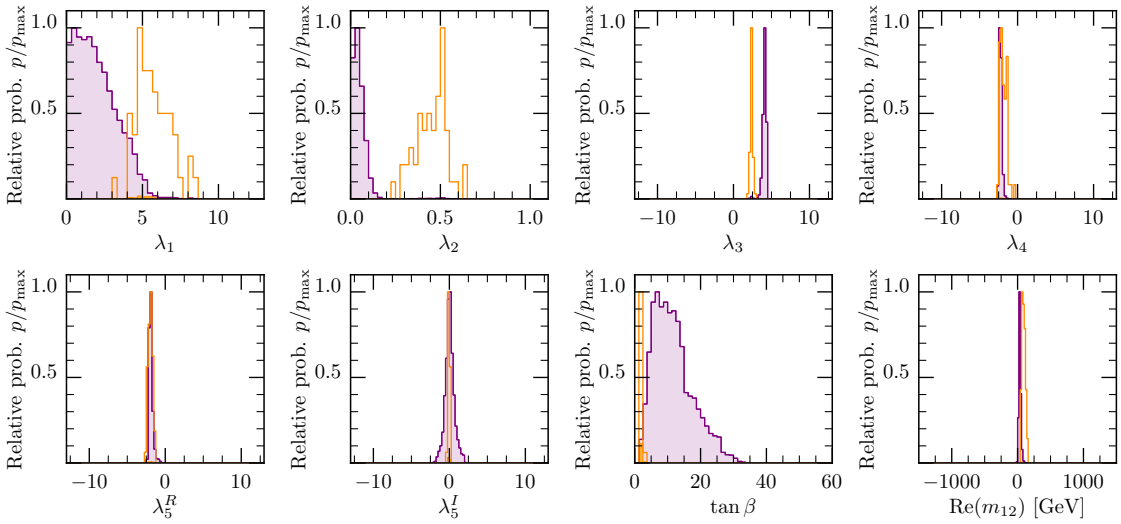

Figure 9. Marginalized posterior distributions for the input parameters in the strong-PT scan. The orange distributions, scaled up for visibility, show the contribution from the scenario where H_1 is the 125 GeV Higgs. To ease comparison with the results in Fig. 2 we choose to still plot λ_5 even though it was replaced by λ_{345} as the input parameter.

λ_1	λ_2	λ_3	λ_4	λ_5^R	λ_5^I	$\tan\beta$	$\mathrm{Re}(m_{12}^2)$	m_{H_1}	m_{H_2}	m_{H_3}	$m_{H^\pm}$
6.40	0.51	2.44	−2.47	−1.73	0.06	2.14	120^2	126	341	344	376
0.64	0.01	4.33	−2.31	−1.95	0.66	7.69	55^2	95	126	352	362

Table 5. Two example points with $\xi_c > 1$ taken from the strong-PT scan. The first point is an example of the standard scenario ($m_{H_1} \approx 125$ GeV), while the second point illustrates the hidden-Higgs scenario ($m_{H_2} \approx 125$ GeV). All masses are given in GeV.

therefore no CP-violating phase. Secondly, when H_1 is the 125 GeV Higgs there is a preference for $\tan\beta$ close to one [24]. In Table 5 we list two example points, one with $m_{H_1} \approx 125$ GeV and one with $m_{H_2} \approx 125$ GeV.

Requiring a strong phase transition has the effect of forcing down the mass scale for the scalars. As seen in Fig. 10, the preferred ranges for all the scalar masses are below 400 GeV. In particular, the predicted range for $m_{H^\pm}$ is below the 490 GeV lower bound for avoiding large contributions to $BR(b \to s\gamma)$. This is illustrated in Fig. 11. The left plot is the posterior distribution for ξ_c, showing that the scan has indeed identified a parameter region giving $\xi_c > 1$. The right plot shows the posterior distribution for $BR(b \to s\gamma)$. The entire range of predicted $BR(b \to s\gamma)$ values is more than 3σ above the observed value, as indicated by the vertical green bands. This demonstrates that the scan was not able to find a parameter region with strong phase transition without accepting significant tension with other observables, thus confirming the result in Fig. 8.

To further illustrate the interplay between the $\xi_c > 1$ requirement and the other constraints we perform two grid scans in the best-fit parameter regions of the strong-PT

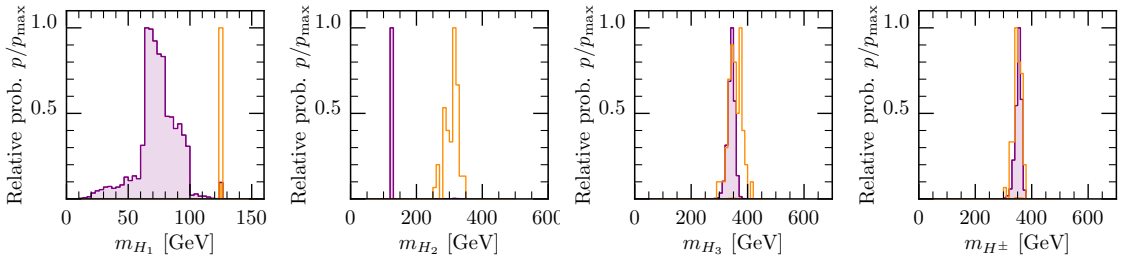

Figure 10. Marginalized posterior distributions for the scalar masses in the strong-PT scan. The posterior contribution from the scenario with H_1 being the 125 GeV Higgs is shown in orange, scaled up for visibility.

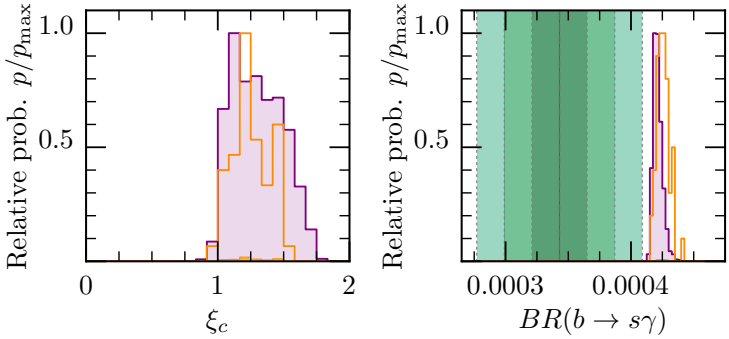

Figure 11. Marginalized posterior distributions for the phase transition strength ξ_c (left) and $BR(b \to s\gamma)$ (right) in the strong-PT scan. The green bands depict the 1σ, 2σ and 3σ regions around the observed value. The contribution from the standard scenario with H_1 as the 125 GeV Higgs is shown in orange, scaled up for visibility.

scan.[14] The first of these two sub-scans is focused on the standard scenario with H_1 as the 125 GeV resonance, while the second sub-scan covers a parameter region in the hidden-Higgs scenario. The scanned parameter planes are defined in Table 6. For the standard scenario we fix the parameters λ_1, λ_3, λ_5^I and $\tan\beta$, take $\lambda_5^R = 0.7\lambda_4$ and scan the plane of λ_4 vs $\mathrm{Re}(m_{12}^2)$. At each point in the plane we choose λ_2 such as to minimize the difference $|m_{H_1} - 125\ \mathrm{GeV}|$. For the hidden-Higgs grid scan we fix λ_1, λ_3, λ_4, λ_5^R and λ_5^I, scan the $\tan\beta$ vs $\mathrm{Re}(m_{12}^2)$ plane and choose λ_2 by minimizing $|m_{H_2} - 125\ \mathrm{GeV}|$. It should be noted that while we always choose λ_2 to minimize $|m_{H_{1,2}} - 125\ \mathrm{GeV}|$, in large regions of the scanned parameter planes this freedom is not enough to actually obtain $m_{H_{1,2}} \approx 125$ GeV.

In Fig. 12 we show the results of the two grid scans, with the scan of the standard scenario in the left-hand plot and the hidden-Higgs scan in the right-hand plot. In both plots there are dark regions marked "unstable" and "unphysical". The "unstable" regions fail the stability requirement detailed in section 4.3, while in the "unphysical" regions spectrum generation fails due to negative squared masses. The other coloured regions depict parameter regions favoured by different constraints: The dark (light) grey regions

[14] These grid scans are not listed in Table 1 as they only serve to highlight some aspects of the strong-PT scan results.

Parameter	Standard scenario	Hidden-Higgs scenario
λ_1	6.5	1.3
λ_2	$\min(\lvert m_{H_1} - 125\text{ GeV}\rvert)$	$\min(\lvert m_{H_2} - 125\text{ GeV}\rvert)$
λ_3	2.5	4.3
λ_4	$[-5, 2]$	-2.3
λ_5^R	$0.7\lambda_4$	-2
λ_5^I	0	0.3
$\tan\beta$	2.2	$[0.5, 50]$
$\mathrm{Re}(m_{12}^2)$	$[-200^2, 500^2]$ GeV^2	$[-100^2, 100^2]$ GeV^2

Table 6. Choice of parameter planes for the grid scans. The 125 GeV Higgs is identified with H_1 in the standard scenario and with H_2 in the hidden-Higgs scenario.

satisfy $\Delta\rho$ at 2σ (3σ), the dark (light) brown regions satisfy $BR(b \to s\gamma)$ at 2σ (3σ) and the purple regions are regions that are allowed at the 95% CL by all the Higgs searches checked by `HiggsBounds`. In the dark (light) orange regions the χ^2 from `HiggsSignals` for the 125 GeV Higgs measurements satisfy $\Delta\chi^2 = \chi^2 - \chi^2_{\text{min}} \leq 6.18$ (11.83), corresponding to 2σ (3σ), where we take χ^2_{min} to be the minimum χ^2 value observed across all the `MultiNest` scans ($\chi^2_{\text{min}} = 75.6,\ \text{ndf} = 81$). Finally, the teal (cyan) regions have a phase transition strength satisfying $\xi_c > 1$ ($\xi_c > 0.5$).

The grid scans illustrate some of the important ways in which the $\xi_c > 1$ constraint determines the preferred parameter regions in the strong-PT scan. First, increasing the mass scale by raising $\mathrm{Re}(m_{12}^2)$ decreases ξ_c. From the right-hand plot we see that this decrease in ξ_c can be counteracted by decreasing $\tan\beta$. This explains the clear preference for low $\tan\beta$ in the standard scenario, as this scenario prefers higher $\mathrm{Re}(m_{12}^2)$ compared to the hidden-Higgs case. Further, in the left-hand plot we see that for a fixed $\mathrm{Re}(m_{12}^2)$ the fit to $BR(b \to s\gamma)$ can be improved by going to large and negative λ_4 and λ_5^R (recall that we have taken $\lambda_5^R = 0.7\lambda_4$), as this increases $m_{H^\pm}$. However, increasing $|\lambda_4|$ and $|\lambda_5^R|$ eventually also affects the masses of H_1 and H_2, causing conflict with both LHC Higgs data and the strong PT requirement. Thus, we end up with a $> 2\sigma$ tension between $\xi_c > 0.5$ and $BR(b \to s\gamma)$. For $\xi_c > 1$ this tension is greater than 3σ. We also note that negative $\mathrm{Re}(m_{12}^2)$ typically gives an unstable potential.

In conclusion we find that the strong-PT scan confirms the result of the main scan, namely that current data does not favour a first-order phase transition in the 2HDM$_5$, and that this result is largely due to the conflict between the low mass scale required for a first-order phase transition and the high $m_{H^\pm}$ required to avoid tension with $BR(b \to s\gamma)$. On the other hand, recent studies of the impact of LHC data on CP-conserving 2HDMs indicate that the hidden-Higgs scenario should be able accomodate charged Higgs masses up to about 600 GeV [77, 79], at which level there would be no significant tension with $BR(b \to s\gamma)$, while still keeping the two lightest scalars around or below 125 GeV. In the next subsection we will investigate the origin of the stricter upper bound on $m_{H^\pm}$ observed in our strong-PT scan. We will find that a $H^\pm$ much lighter than 600 GeV is in fact a general consequence of the hidden-Higgs scenario and the loop-level spectrum calculation

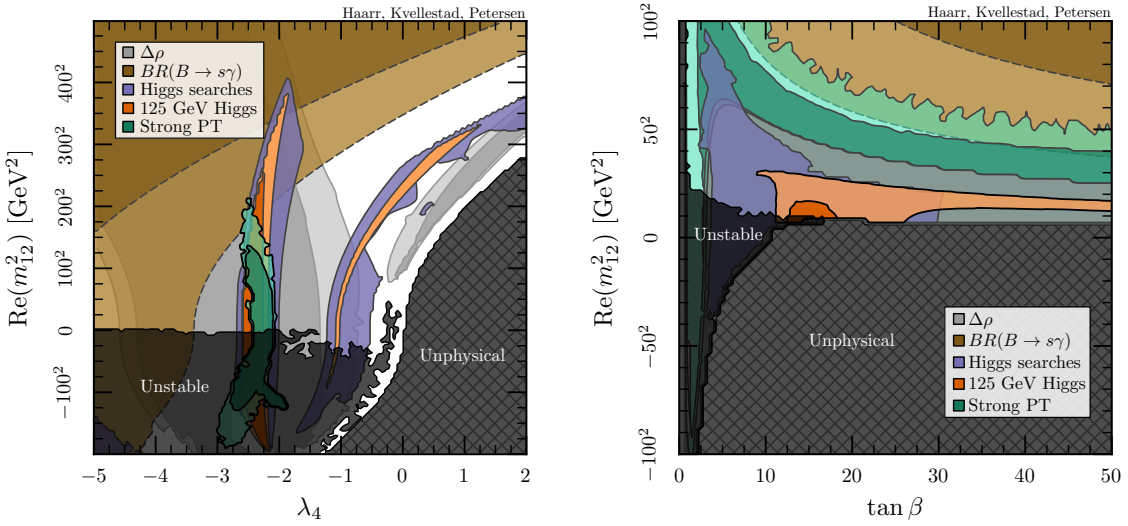

Figure 12. Lower-dimensional grid scans exhibiting regions of strong electroweak phase transition. *Left:* The plane of λ_4 vs $\mathrm{Re}(m_{12}^2)$, with the remaining parameters chosen according to the "standard scenario" in Table 6. *Right:* The plane of $\tan\beta$ vs $\mathrm{Re}(m_{12}^2)$, with the other parameters set to the hidden-Higgs scenario in Table 6. Dark regions marked "unstable" and "unphysical" fail the stability condition and have negative squared masses, respectively. The other coloured regions depict the following: *Teal (cyan):* Phase transition strength satisfying $\xi_c > 1$ ($\xi_c > 0.5$). *Dark (light) orange:* Within 2σ (3σ) of the best-fit point for the 125 GeV Higgs data. *Purple:* Allowed at the 95% CL by collider searches for additional Higgs bosons. *Dark (light) brown:* Predicted $BR(b \to s\gamma)$ within 2σ (3σ) of the observed value. *Dark (light) grey:* Predicted $\Delta\rho$ within 2σ (3σ) of the observed value.

we employ.

Finally, we remind the reader that any constraints coming from processes involving Yukawas are type dependent. In particular, the constraint from $BR(b \to s\gamma)$ on the type-I model is less severe than for the type-II case that we study here. In the $\mathrm{2HDM}_5$ with type-I couplings, the effect of this constraint is to tune the charged Higgs mass to $m_{H^\pm} \sim v \approx 246$ GeV [24]. Furthermore, some parameter regions in the type-I model seem to provide interesting possibilities for detection at the LHC [25].

5.2 A closer look at the hidden-Higgs scenario

Even if no requirement is put on the phase transition strength, an upper bound on the heavy scalar masses arises in the hidden-Higgs scenario due to the limited parametric freedom: After requiring EWSB with $v \approx 246\,\mathrm{GeV}$, the only free mass scale in the theory is $\sqrt{|\,\mathrm{Re}(m_{12}^2)|}$. In the standard scenario, where H_1 is SM-like, v sets the correct mass scale for $m_{H_1} \approx 125$ GeV. The free parameter $\mathrm{Re}(m_{12}^2)$ can then be used to push the remaining scalars up to a high mass scale, as seen in the main scan in Sec. 5. This scale separation is no longer possible in the hidden-Higgs scenario due to the stronger requirement of having $m_{H_1} < m_{H_2} \approx 125$ GeV. A large mass gap up to H_3 and $H^\pm$ then relies on having large quartic couplings, meaning that constraints on these couplings translate into upper bounds

Priors and settings for the hidden-Higgs scans

Parameter	Range	Type	`MultiNest` setting	Value
λ_1	$[0, 4\pi]$	flat	`nlive`	2000
λ_2	$[0, 1]$	flat	`tol`	0.5
λ_3	$[-4\pi, 4\pi]$	flat	`efr`	0.8
λ_4	$[-4\pi, 4\pi]$	flat	Likelihood	Included
λ_{345}	$[-5, 5]$	flat	Stability	Yes
λ_5^I	$[-4\pi, 4\pi]$	flat	Direct searches	Yes
$\tan\beta$	$[0.1, 60]$	flat	$\Delta\rho$ + B physics	Yes
$\mathrm{Re}(m_{12}^2)$	$[-500^2, 500^2]$ GeV^2	two-sided log	Strong PT	No
			Sampled points	Posterior
			1.6×10^7	1.1×10^4

Table 7. Prior distributions, likelihood contributions and `MultiNest` settings for the tree-level and loop-level hidden-Higgs scans. For the tree-level scan the stability requirement in the likelihood refers to the check of global minimum and positivity of the tree-level scalar potential as in [20, 80]. The number of visited points and posterior samples refer to the loop-level scan. The tree-level scan visited around 1.1×10^7 points, producing 9.5×10^3 posterior samples.

on m_{H_3} and $m_{H^\pm}$. We note that increasing $\tan\beta$ will also help raise $m_{H^\pm}$ through the first term in Eq. (2.12), but this effect is sub-dominant when $\mathrm{Re}(m_{12}^2) < v^2$.

In the CP-conserving type-II model studied in Ref. [77], the light CP-even h^0 is the hidden state and the heavy CP-even H^0 plays the role of the 125 GeV Higgs. The study identifies constraints on the scalar masses and the mixing of the CP-even states coming from the 7 and 8 TeV LHC data. A similar analysis, focused on deriving constraints on the scalar potential parameters, is presented in Ref. [79]. The authors of [79] analyse a set of parameter points drawn from flat probability distributions in the real parameters $\lambda_{1,2,3,4,5}$, $\tan\beta$ and m_{12}^2, discarding points that are in significant tension with any of the applied experimental constraints. While no statistical fit is performed, the surviving set of parameter points indicate that the SM alignment required by the LHC Higgs results impose an upper bound on the masses of $H^\pm$ and A^0 of $m_{H^\pm, A^0} \lesssim 600$ GeV, similar to what is found in [77].

For our investigation of the hidden-Higgs scenario we scan the relevant subspace of the 2HDM$_5$ parameter space with `MultiNest`, using the likelihood function described in Sec. 4.2. Thus, in the following we do not include any constraint on the phase transition strength. In [79] the scalar spectrum is calculated at tree level from the input parameters. To compare our results against this analysis we run two separate scans, one in which we switch off the loop corrections in `SPheno` and one where the loop corrections are included. In the following we refer to these scans individually as the "tree-level scan" and "loop-level scan", and collectively as the "hidden-Higgs scans".

The scan setup is summarized in Table 7. Note that the stability check for the tree-level scan involves checking for global minimum and positivity using inequalities from [80] and [20]. As for the strong-PT scan, we restrict the prior for λ_2 to the range $[0, 1.0]$ and take λ_{345} as an input parameter instead of λ_5^R. Further, the prior range for $\mathrm{Re}(m_{12}^2)$ is

limited to $[-500^2, 500^2]$ GeV^2. To ensure that we only scan the hidden-Higgs scenario we impose the additional hard constraint that $m_{H_1} < 120$ GeV. Thus, our overall effective prior is

$$\pi(\boldsymbol{\Theta}) = H\left(1 - \frac{m_{H_1}(\boldsymbol{\Theta})}{120\,\text{GeV}}\right)\prod_j \pi_j(\theta_j), \tag{5.4}$$

where π_j are the priors for the individual input parameters θ_j.

As previously discussed, we have not imposed the tree-level perturbative unitarity constraint [63] in our scans. While relatively unimportant for the previous scans, this constraint significantly impacts the hidden-Higgs scans presented here. To illustrate this we present two sets of posterior results, one with the posteriors resulting from our scans and one where we have discarded posterior samples that violate perturbative unitarity. In the tree-level analysis in [79] the perturbative unitarity constraint is included in the scan. Also, in contrast to our analysis, the requirement that the vacuum is a global minimum of the potential is not imposed.

In the upper two rows of Fig. 13 we show the posterior results of the tree-level (orange) and loop-level (brown) scans. The bottom two rows (darker colours) contain the same posterior distributions after requiring tree-level perturbative unitarity. Focusing first on the tree-level scan, we find that the preferred parameter ranges show good agreement with the parameter bounds for the type-II CP-conserving model in [79], in particular after taking into account the perturbative unitarity constraint. The main difference is that our posterior distributions are somewhat broader compared to the results in [79]. This is to be expected from the difference in methodology and the additional freedom in our model coming from the extra λ_5^I parameter.

The posterior distributions for the tree-level m_{H_1}, m_{H_3} and $m_{H^\pm}$ are shown in Fig. 14 (orange). Our preferred ranges for the scalar masses agree well with the results that [79] find for m_{h^0}, m_{A^0} and $m_{H^\pm}$. Two bounds on the preferred mass ranges are worth commenting: First, we see the same upper bound on $m_{H^\pm}$ around 600 GeV as in [77, 79]. This is a consequence of an interplay between the LHC Higgs data and the perturbativity bound of $\lambda_3 < 4\pi$: At tree level the LHC Higgs data prefers small values of λ_{345}. This can be seen in Fig. 15 and is also found in [79]. At the same time, $BR(b \to s\gamma)$ requires a large $m_{H^\pm}$. With $\text{Re}(m_{12}^2)$ constrained by the requirement of having both H_1 and H_2 light, the tree-level $m_{H^\pm}$ can only be pushed up by large and negative $(\lambda_4 + \lambda_5)$, see Eq. (2.12). The combined effect of the $\lambda_{345} \sim 0$ preference and the perturbativity bound is then $\lambda_3 \sim -(\lambda_4 + \lambda_5^R) < 4\pi$, which gives the upper bound on $m_{H^\pm}$. Second, we see a clear preference for $m_{H_1} > m_{H_2}/2 \approx 62.5$ GeV. Below this mass the decay channel $H_2 \to H_1 H_1$ opens up, which quickly leads to conflict with the observed Higgs data.[15] This effect is also observed in [77, 79].

We now move on to the result of the loop-level scan. As seen from Fig. 13 (brown distributions), calculating the spectrum at one-loop order leads to a preference for smaller magnitudes of λ_3, λ_4 and λ_5^R compared to the result of the tree-level scan. This can be

[15] See Ref. [81] for a dedicated study of the viability of parameter regions with $m_{H_1} < m_{H_2}/2$.

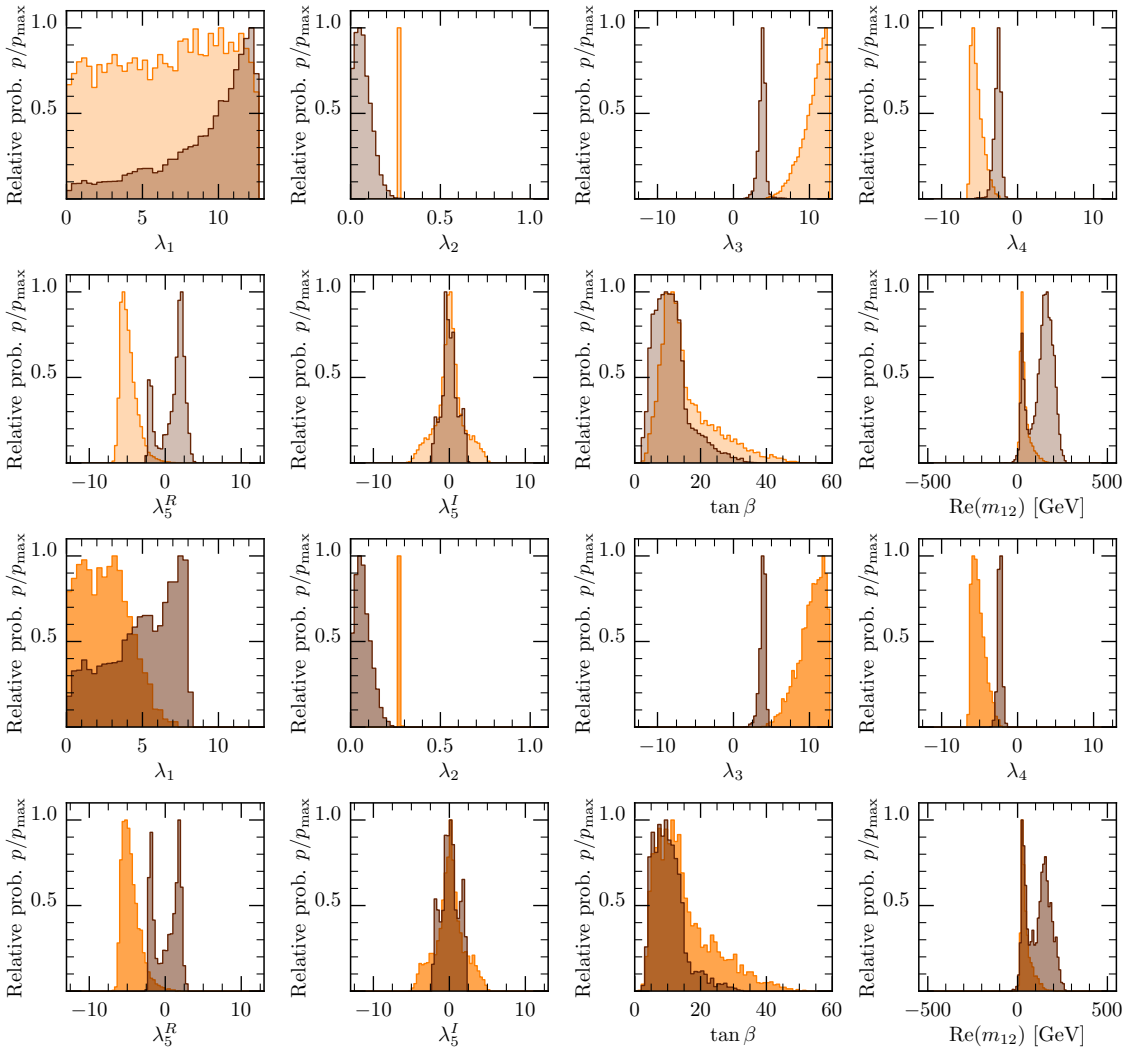

Figure 13. Marginalized posterior distributions for the parameters in the hidden-Higgs scans. *Top two rows:* The parameter posteriors resulting from the tree-level scan (orange) and loop-level scan (brown). *Bottom two rows:* The same posterior distributions after discarding samples that fail the tree-level perturbative unitarity constraint.

understood as follows: In the tree-level case, the dependence of m_{H_1}, m_{H_2} on λ_4 and λ_5^R can be cancelled by adjusting λ_3 such that λ_{345} remains constant. Thus, $m_{H^\pm}$ can be pushed up without affecting m_{H_1} and m_{H_2}. This is no longer true for the one-loop masses, with the consequence that the hidden-Higgs scenario $m_{H_1} < m_{H_2} \approx 125$ GeV is confined to a smaller range in the quartic couplings. We illustrate this in Fig. 16. Here we plot the scalar masses as functions of $\lambda_3 = -\frac{9}{5}\lambda_4 = -\frac{9}{4}\lambda_5^R$ while fixing all other parameters. This choice ensures a constant $\lambda_{345} = 0$, meaning that λ_5^R is the only non-constant contribution to the tree-level masses through the term $(\mathcal{M}^2)_{33} = \mu^2 - v^2\lambda_5^R$ in Eq. (2.9). Thus, the two lightest tree-level masses (blue and red dotted lines) remain constant with increasing $|\lambda_5^R|$. The tree-level masses are plotted for $\lambda_2 = 0.26$ which gives $m_{H_2} \approx 125$ GeV. The one-loop

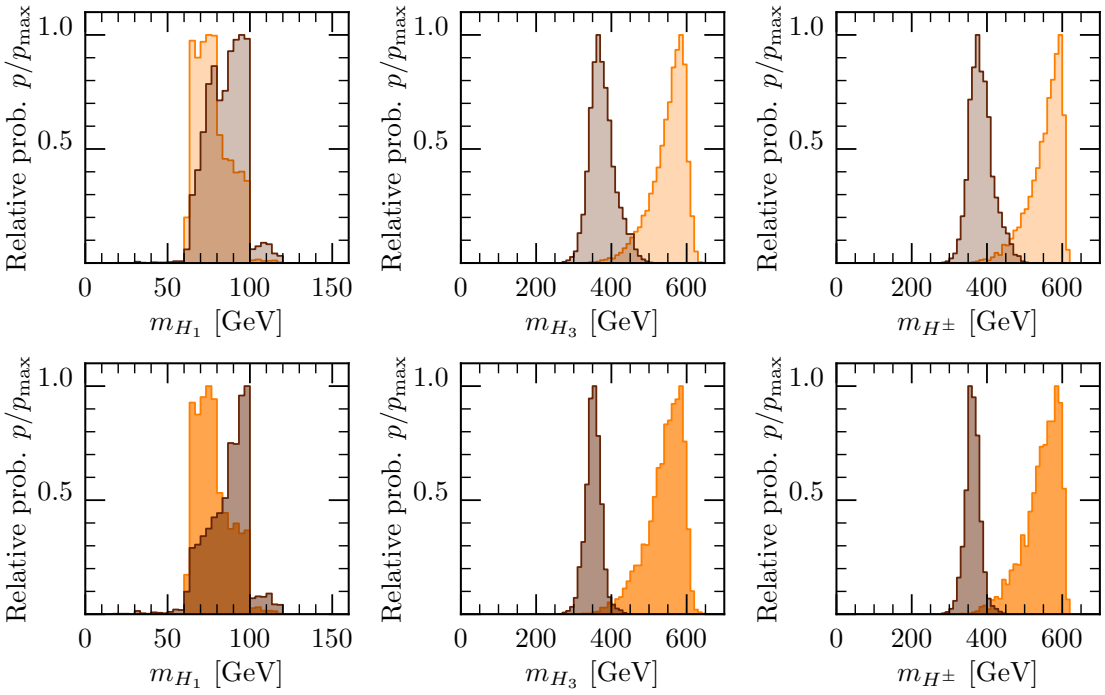

Figure 14. Marginalized posterior distributions for m_{H_1}, m_{H_3} and $m_{H^\pm}$. *Top row:* The posteriors resulting from the tree-level scan (orange) and loop-level scan (brown). *Bottom row:* The same distributions after discarding samples that fail the tree-level perturbative unitarity constraint.

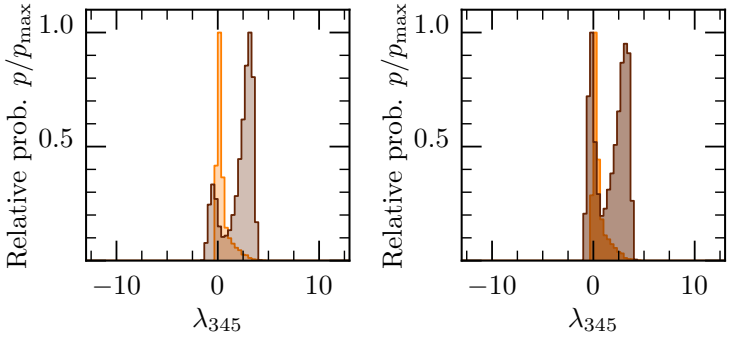

Figure 15. *Left:* Marginalized posterior distributions for $\lambda_{345} \equiv \lambda_3 + \lambda_4 + \lambda_5^R$ from the tree-level scan (orange) and the loop-level scan (brown). *Right:* The same distribution after requiring tree-level perturbative unitarity.

masses for the same λ_2 value are shown as solid lines. In this case m_{H_2} exceeds 125 GeV already for $\lambda_3 \approx 2$, corresponding to $\lambda_4 \approx -1.1$ and $\lambda_5^R \approx -0.9$. By taking $\lambda_2 \to 0$ the departure of the one-loop m_{H_2} can be delayed somewhat. For instance, setting $\lambda_2 = 0$ in the scenario plotted in Fig. 16 (dashed lines) extends the $m_{H_2} \lesssim 125$ GeV region up to $\lambda_3 \approx 4$, corresponding to $\lambda_4 \approx -2.2$ and $\lambda_5^R \approx -1.8$. (Note that in this case a slightly larger $\mathrm{Re}(m_{12}^2)$ would be needed to obtain $m_{H_2} \approx 125$ GeV in the region of small λ_3.)

An additional hidden-Higgs parameter region, with $\lambda_5^R > 0$, opens up at loop level. A

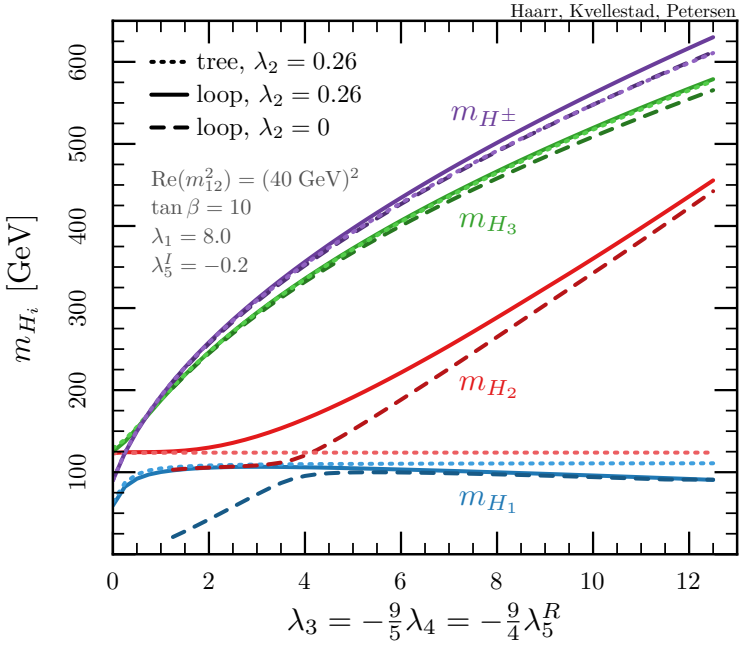

Figure 16. A comparison of the scalar masses as functions of $\lambda_3 = -\frac{9}{5}\lambda_4 = -\frac{9}{4}\lambda_5^R$. The dotted and solid lines depict tree-level and one-loop masses respectively, for $\lambda_2 = 0.26$. The dashed lines show one-loop masses for $\lambda_2 = 0$. The remaining parameters are set as follows: $\lambda_1 = 8.0$, $\lambda_5^I = -0.2$, $\tan\beta = 10$, $\mathrm{Re}(m_{12}^2) = (40\ \mathrm{GeV})^2$.

positive λ_5^R reduces $m_{H^\pm}$, but this reduction is compensated by an increase in $\mathrm{Re}(m_{12}^2)$. This parameter region manifests as distinct peaks centred at $\lambda_5^R \approx 2$ and $\mathrm{Re}(m_{12}^2) \approx (150\ \mathrm{GeV})^2$ in the loop-level scan posteriors in Fig. 13, and a corresponding peak at $\lambda_{345} \approx 3$ in Fig. 15. With $\lambda_5^R > 0$ the hidden-Higgs scenario can extend towards larger $|\lambda_4|$, evident as a tail towards $\lambda_4 \approx -5$ in the upper right-hand plot of Fig. 13. These parameter choices produce an unstable tree-level scalar potential, which explains why this region is not present in the tree-level scan results. In the loop-level scan this parameter region can survive the stability check for the one-loop potential described in Sec. 4.3, especially for large λ_1.[16] However, large λ_1 values conflicts with the tree-level perturbative unitarity constraint, as can be seen in the bottom two rows of Fig. 13. Thus, the relative posterior weight for this parameter region is reduced when perturbative unitarity is required.

In summary, the loop-level dependence of m_{H_1},m_{H_2} on λ_4 and λ_5^R, along with the stability and perturbative unitarity constraints, restrict the hidden-Higgs scenario to parameter regions with $m_{H^\pm}$ much below the 600 GeV bound observed at tree-level. This can be seen in the posterior for the one-loop $m_{H^\pm}$ in the upper right-hand plot of Fig. 14 (brown). The preferred $m_{H^\pm}$ range resulting from the loop-level scan extends up to $m_{H^\pm}$ just below 500 GeV. The upper tail of the $m_{H^\pm}$ distribution is associated with the $\lambda_5^R > 0$, $\mathrm{Re}(m_{12}^2) \gtrsim (100\ \mathrm{GeV})^2$ parameter region described above. Imposing tree-level

[16] Note that the numerical stability check of $V(\eta_1, \eta_2, \eta_3)$ in Sec. 4.3 is limited in field space to the region $|\eta_i| < 20 m_t$, whereas the inequalities used to check positivity of $V_{\mathrm{tree}}(\eta_1, \eta_2, \eta_3)$ are derived from the limit $|\eta_i| \to \infty$.

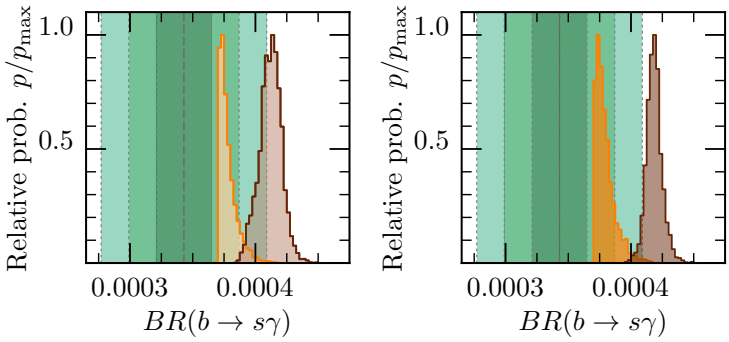

Figure 17. *Left:* Marginalized posterior distributions for $BR(b \to s\gamma)$ from the tree-level (orange) and loop-level (brown) scans. *Right:* The same distributions after discarding samples that fail the tree-level perturbative unitarity constraint. The green bands show the 1σ, 2σ and 3σ regions around the observed value.

perturbative unitarity cuts into this parameter region, with the result that the preferred $m_{H^\pm}$ range is restricted to $m_{H^\pm} < 440$ GeV (lower right-hand plot). For the $\lambda_5^R < 0$, $\mathrm{Re}(m_{12}^2) \lesssim (100\ \mathrm{GeV})^2$ region also found in the tree-level scan, the probable range for the loop-level $m_{H^\pm}$ is limited to $m_{H^\pm} < 400$ GeV.

So while at tree level the best-fit region for the hidden-Higgs scenario stays clear of strong tension with the observed $BR(b \to s\gamma)$, this is no longer true at loop level. We illustrate this in Fig. 17 by comparing the posteriors for $BR(b \to s\gamma)$ from the tree-level (orange) and loop-level (brown) scans to the 3σ range for the observed value. The preferred range for $BR(b \to s\gamma)$ in the loop-level scan see a $\gtrsim 2\sigma$ tension with the observed value (left-hand plot). This tension is further strengthened when perturbative unitarity is required (right-hand plot).

6 Conclusions

In this study we have performed a series of Bayesian fits of the 2HDM$_5$ with type-II Yukawa couplings. Our main aim has been to investigate how current experimental constraints affect the probability for a strong first-order phase transition. We find that fitting the model to the 125 GeV Higgs data, collider searches for additional Higgs bosons, the electroweak precision observable $\Delta\rho$ and a selection of B-physics observables severly lowers this probability.

The above conclusion has been checked by means of an additional fit where we constrain the model to regions of parameter space with a first-order phase transition. This is done by including the requirement $\xi_c > 1$ as a 95% CL lower limit in the likelihood function. This requirement introduces a strong preference for light scalar masses, with the consequence that the best-fit region is dominated by the "hidden-Higgs" scenario. In this scenario the next-to-lightest scalar, H_2, is the 125 GeV Higgs and the lighter state H_1 has remained undetected. In comparison, the standard Higgs scenario with H_1 as the 125 GeV state only accounts for about 1% of the posterior probability in this fit. The two scenarios have characteristics that agree with previously studied models of baryogenesis in 2HDMs: First,

we see no indication that a non-zero CP-violating phase is important to obtain a first-order transition. Second, we find a preference for small $\tan\beta$ when H_1 is the 125 GeV state.

The insistence of $\xi_c > 1$ in the likelihood forces the model into a part of parameter space where there is significant tension with experimental constraints: Whereas a first-order phase transition prefers a low mass scale for the additional scalars, a $m_{H^\pm}$ heavier than about 490 GeV is required for the predicted $BR(b \to s\gamma)$ to stay within 2σ of the observed value. With only one free mass parameter in the theory, $\mathrm{Re}(m_{12}^2)$, a large mass splitting between $H^\pm$ and the lighter $H_{1,2}$ can only be achieved by going to large values in the quartic couplings, but this brings the model into conflict data on the 125 GeV Higgs. This tension between the experimental constraints and the $\xi_c > 1$ requirement confirms the conclusion that a first-order phase transition is not a likely prediction of the type-II 2HDM$_5$.

For similar reasons we find that the hidden-Higgs scenario in the type-II 2HDM$_5$ is disfavoured by current data, regardless of the phase transition strength: The requirement that $m_{H_1} < m_{H_2} \approx 125$ GeV forces down the mass scale $\mathrm{Re}(m_{12}^2)$, with the consequence that the masses of the heavier scalars get bounded from above by constraints on the quartic couplings. With tree-level spectrum calculation this upper bound on m_{H_3} and $m_{H^\pm}$ is around 600 GeV and is a consequence of the perturbativity bound $\lambda_3 < 4\pi$. However, when the mass spectrum is calculated at one loop we find that the preferred parameter region has $m_{H_3}, m_{H^\pm} < 500$ GeV. This stronger upper bound is a consequence of the stability condition for the one-loop effective potential, and the fact that at one-loop order, increasing $-(\lambda_4 + \lambda_5^R)$ to raise $m_{H^\pm}$ eventually also causes $m_{H_2} > 125$ GeV, in conflict with the LHC data. Further, if tree-level perturbative unitarity is required we find that $m_{H_3}, m_{H^\pm} < 440$ GeV is preferred. As a result of these loop-level bounds on $m_{H^\pm}$ there is significant tension between the predictions of the hidden-Higgs scenario and the experimental data, most notably $BR(b \to s\gamma)$.

We end by mentioning a few ways in which the current study can be further improved and expanded. First, the likelihood function can be extended to include contributions from more observables, most importantly LHC Higgs results at 13 TeV, a more complete set of flavour observables and electric dipole moments. Further, the check for stability of the scalar potential can be made more sophisticated by also accepting parameter points for which the broken minimum is metastable. Also, using `SARAH` and `SPheno`, we can implement the RG-improved effective potential as in [29]. This could in turn enable an extension of the stability check by requiring the potential to remain stable also at scales higher than the electroweak scale, similar to what was done in [82]. Finally, the accuracy with which the posterior distributions have been determined should ideally be improved by running `MultiNest` with a higher number of live points and stricter convergence criteria, in particular for the fit with $\xi_c > 1$ included in the likelihood. Given enough CPU time this would also enable a frequentist analysis in terms of profile likelihoods, to serve as a useful comparison to the Bayesian analysis presented here.

In future work we plan to extend the current analysis to 2HDMs with other Yukawa structures.

Acknowledgements

We thank Anders Tranberg for useful discussions and valuable input. Also, we thank Florian Staub for help with using the `SARAH/SPheno` interface. In this work we made extensive use of the `PySLHA` [83] package to ease communication between the different numerical tools, and the `pippi` [84] package for plotting posterior distributions. The CPU intensive parameter scans in this work was carried out using the Abel Cluster, owned by the Norwegian metacenter for High Performance Computing (NOTUR) and the University of Oslo. The computing time was made available through NOTUR allocation NN9284K, financed through the Research Council of Norway. AH and AK thank the Niels Bohr Institute for generous hospitality while part of this work was completed.

A Field- and temperature-dependent masses

A.1 Neutral scalars

The tree-level Higgs mass matrix gets a debye-corrected mass matrix [14]:

$$\delta m_{ij}^2 = \frac{T^2}{24} \sum_k N_k \frac{\partial^2 m_k^2(\phi_n)}{\partial\phi_i \partial\phi_j} \tag{A.1}$$

where in our case $\phi_i = \eta_i$, for $i = 1, 2, 3$ and $\phi_4 = \mathrm{G}_0$. The m_k^2 are the zero-temperature, field-dependent masses of the relevant particles, see Eq. (3.3). For the Higgs-sector the calculation is significantly simplified by utilizing that the sum of neutral-squared masses equals the trace of the tree-level mass matrix.[17] The total four-by-four, field- and temperature-dependent mass matrix is:

$$\mathcal{N}_{ij}^2 = \mathcal{M}_{ij}^2 + \delta m_{ij}^2 \tag{A.2}$$

with components given by:

$$\begin{aligned}
\mathcal{N}^2_{\eta_1,\eta_1} = \frac{1}{2}\Big(& \eta_3^2\lambda_1 \sin^2\beta + 2\mu^2 \sin^2\beta + 3\eta_1^2\lambda_1 + \eta_2^2\lambda_3 + \eta_2^2\lambda_4 \\
& - 2\cos\beta\left(\eta_3\lambda_5^I\left(\eta_2 + v\sin\beta\right) - 3\eta_1\lambda_1 v\right) + \eta_2^2\lambda_5^R \\
& + \cos^2\beta\left(\eta_3^2\left(\lambda_3 + \lambda_4 - \lambda_5^R\right) + 2\lambda_1 v^2\right) + 2\eta_2 v\sin\beta\left(\lambda_3 + \lambda_4 + \lambda_5^R\right)\Big) \\
& + \frac{1}{24}T^2\left[\frac{9g^2}{2} + \frac{3g\prime^2}{2} + 6\lambda_1 + 4\lambda_3 + 2\lambda_4 - \frac{24m_b^2}{v^2\cos^2\beta}\right]
\end{aligned} \tag{A.3}$$

[17] The trace is basis independent. This can be seen using its cyclic property, which cancels the rotation matrices.

$$\begin{aligned}\mathcal{N}^2_{\eta_2,\eta_2} = \frac{1}{2}\Bigg(& \eta_3^2\lambda_3\sin^2\beta + \eta_3^2\lambda_4\sin^2\beta + 2\mu^2\cos^2\beta \\ & + 2\eta_1\left(-\eta_3\sin\beta\lambda_5^I + v\cos\beta\lambda_5^R + \lambda_3 v\cos\beta + \lambda_4 v\cos\beta\right) \\ & - 2\eta_3 v\sin\beta\cos\beta\lambda_5^I - \eta_3^2\sin^2\beta\lambda_5^R + \eta_1^2\left(\lambda_3+\lambda_4+\lambda_5^R\right) \\ & + \lambda_2\left(\eta_3^2\cos^2\beta + 3\eta_2^2 + 2v^2\sin^2\beta + 6\eta_2 v\sin\beta\right)\Bigg) \\ & + \frac{1}{24}T^2\left[\frac{9g^2}{2} + \frac{3g'^2}{2} + 6\lambda_2 + 4\lambda_3 + 2\lambda_4 - \frac{24m_t^2}{v^2\sin^2\beta}\right]\end{aligned} \tag{A.4}$$

$$\begin{aligned}\mathcal{N}^2_{\eta_3,\eta_3} = & \left(\frac{\eta_1}{2}\Bigg[\cos\beta\Bigg(3\eta_3\sin 2\beta\lambda_5^I - 4\eta_2\sin\beta\lambda_5^R\right. \\ & + v\cos 2\beta\lambda_5^R - 3v\lambda_5^R + 2\lambda_3 v\cos^2\beta + 2\lambda_4 v\cos^2\beta\Bigg) \\ & \left. + \lambda_1 v\sin\beta\sin 2\beta\Bigg] + \frac{3}{2}\eta_3\sin 2\beta\lambda_5^I\left(\eta_2\sin\beta + v\right)\right. \\ & + \frac{3}{4}\eta_3^2\left(2\lambda_1\sin^4\beta + 2\lambda_2\cos^4\beta + \sin^2 2\beta\left(\lambda_3+\lambda_4+\lambda_5^R\right)\right) \\ & + \frac{1}{2}\eta_1^2\left(\lambda_1\sin^2\beta + \cos^2\beta\left(\lambda_3+\lambda_4-\lambda_5^R\right)\right) \\ & + \frac{1}{2}\Bigg[\eta_2^2\left(\lambda_2\cos^2\beta + \sin^2\beta\left(\lambda_3+\lambda_4-\lambda_5^R\right)\right) + 2\left(\mu^2 - v^2\lambda_5^R\right) \\ & + 2\eta_2 v\sin\beta\left(\lambda_3\sin^2\beta + \lambda_4\sin^2\beta + \lambda_2\cos^2\beta - \sin^2\beta\lambda_5^R - 2\cos^2\beta\lambda_5^R\right)\Bigg]\Bigg) \\ & + \frac{T^2}{24} \\ & \times\left(\Bigg[\left(6\lambda_1\sin^2\beta + 6\lambda_2\cos^2\beta + \frac{9}{2}g^2 + \frac{3}{2}g'^2 + 4\lambda_3 + 2\lambda_4\right)\right. \\ & \left. - 24\frac{m_b^2}{v^2}\tan^2\beta - 24\frac{m_t^2}{v^2}\cot^2\beta\Bigg]\right)\end{aligned} \tag{A.5}$$

$$\tag{A.6}$$

$$\begin{aligned}\mathcal{N}^2_{\mathrm{G}_0,\mathrm{G}_0} = & \frac{1}{2}\sin^2\beta\Bigg(2\eta_1\Bigg[\eta_3\sin\beta\lambda_5^I - 2\eta_3\cos\beta\cot\beta\lambda_5^I + 2\eta_2\cot\beta\lambda_5^R \\ & + v\cos\beta\lambda_5^R + \lambda_3 v\cos\beta + \lambda_4 v\cos\beta + \lambda_1 v\cos\beta\cot^2\beta\Bigg] \\ & + \eta_3\cot\beta\csc\beta\lambda_5^I\left(\eta_2(3\cos 2\beta - 1) - 2v\sin\beta\right) + \eta_1^2\left(\lambda_1\cot^2\beta + \lambda_3 + \lambda_4 - \lambda_5^R\right) \\ & + \frac{1}{4}\eta_3^2\csc^2\beta\left(3\lambda_1\sin^2 2\beta + 3\lambda_2\sin^2 2\beta + (3\cos 4\beta + 1)\left(\lambda_3+\lambda_4+\lambda_5^R\right)\right) \\ & + \eta_2\Bigg[\cot^2\beta\left(\lambda_5^R\left(2v\sin\beta - \eta_2\right) + \lambda_3\left(\eta_2 + 2v\sin\beta\right) + \lambda_4\left(\eta_2 + 2v\sin\beta\right)\right) \\ & + \lambda_2\left(\eta_2 + 2v\sin\beta\right)\Bigg]\Bigg) \\ & + \frac{T^2}{24}\left[6\lambda_2\sin^2\beta + 6\lambda_1\cos^2\beta + \frac{9g^2}{2} + \frac{3g'^2}{2} + 4\lambda_3 + 2\lambda_4 - \frac{24m_b^2}{v^2} - \frac{24m_t^2}{v^2}\right]\end{aligned} \tag{A.7}$$

$$\mathcal{N}^2_{\eta_1,\eta_2} = \frac{1}{2}\Big(-\mu^2 \sin 2\beta - 2\eta_2\eta_3 \sin\beta\lambda_5^I - 2\eta_1\eta_3\cos\beta\lambda_5^I - 2\eta_3 v\lambda_5^I \tag{A.8}$$
$$- \eta_3^2 \sin 2\beta\lambda_5^R + 2\eta_1\eta_2\lambda_5^R + v^2 \sin 2\beta\lambda_5^R + 2\eta_1 v \sin\beta\lambda^r{}_5 + 2\eta_2 v\cos\beta\lambda_5^R$$
$$+ 2\lambda_3(\eta_2 + v\sin\beta)(\eta_1 + v\cos\beta) + 2\lambda_4(\eta_2 + v\sin\beta)(\eta_1 + v\cos\beta)\Big)$$

$$\mathcal{N}^2_{\eta_1,\eta_3} = \frac{1}{2}\Big(3\eta_3^2 \sin\beta\cos^2\beta\lambda_5^I - \lambda_5^I\Big[\eta_2^2\sin\beta + v^2\sin\beta \tag{A.9}$$
$$+ 2\eta_1\cos\beta(\eta_2 + v\sin\beta) + 2\eta_2 v\Big]$$
$$+ \eta_3\Big[\cos\beta\Big(\lambda_5^R(-4\eta_2\sin\beta - 2\eta_1\cos\beta + v(\cos 2\beta - 3))$$
$$+ 2\lambda_3\cos\beta(\eta_1 + v\cos\beta)$$
$$+ 2\lambda_4\cos\beta(\eta_1 + v\cos\beta)\Big) + 2\lambda_1\sin^2\beta(\eta_1 + v\cos\beta)\Big]\Big)$$

$$\mathcal{N}^2_{\eta_1,\mathrm{G}_0} = \frac{1}{8}\Big(\eta_3^2(-(\cos\beta + 3\cos 3\beta))\lambda_5^I + 4\lambda_5^I\left(\eta_2^2\cos\beta - 2\eta_1\sin\beta(\eta_2 + v\sin\beta)\right) \tag{A.10}$$
$$+ 2\eta_3\Big[2\eta_1\lambda_4\sin 2\beta - 2\eta_1\sin 2\beta\lambda_5^R + 4\eta_2\cos 2\beta\lambda_5^R - 3v\sin\beta\lambda_5^R + v\sin 3\beta\lambda_5^R$$
$$- 2\lambda_1\sin 2\beta(\eta_1 + v\cos\beta) + 2\lambda_3\sin 2\beta(\eta_1 + v\cos\beta) + \lambda_4 v\sin\beta + \lambda_4 v\sin 3\beta\Big]\Big)$$

$$\mathcal{N}^2_{\eta_2,\eta_3} = \frac{1}{2}\Big(3\eta_3^2\sin^2\beta\cos\beta\lambda_5^I \tag{A.11}$$
$$- \lambda_5^I\Big[\eta_1^2\cos\beta + 2\eta_1(\eta_2\sin\beta + v) + v\cos\beta(2\eta_2\sin\beta + v)\Big]$$
$$+ \eta_3\Big[\sin\beta\Big(-\lambda_5^R(2\eta_2\sin\beta + 4\eta_1\cos\beta + v(\cos 2\beta + 3)) + 2\lambda_3\sin\beta(\eta_2 + v\sin\beta)$$
$$+ 2\lambda_4\sin\beta(\eta_2 + v\sin\beta)\Big) + 2\lambda_2\cos^2\beta(\eta_2 + v\sin\beta)\Big]\Big)$$

$$\mathcal{N}^2_{\eta_2,\mathrm{G}_0} = \frac{1}{8}\Big(\eta_3^2(\sin\beta - 3\sin 3\beta)\lambda_5^I + 4\lambda_5^I\left(-\eta_1^2\sin\beta + 2\eta_1\eta_2\cos\beta + 2\eta_2 v\cos^2\beta\right) \tag{A.12}$$
$$- 4\eta_3\Big[\eta_2\lambda_4\sin 2\beta + 2\eta_1\sin^2\beta\lambda_5^R - \eta_2\sin 2\beta\lambda_5^R - 2\eta_1\cos^2\beta\lambda_5^R - 2v\cos^3\beta\lambda_5^R$$
$$- \lambda_2\sin 2\beta(\eta_2 + v\sin\beta) + \lambda_3\sin 2\beta(\eta_2 + v\sin\beta) + \lambda_4 v\sin\beta\sin 2\beta\Big]\Big)$$

$$
\begin{aligned}
\mathcal{N}^2_{\eta_3,\mathrm{G}_0} = \frac{1}{8}\Bigg(& 2\eta_1\Big[-\eta_3\cos\beta\lambda_5^I - 3\eta_3\cos 3\beta\lambda_5^I + 4\eta_2\cos 2\beta\lambda_5^R - 3v\sin\beta\lambda_5^R \\
&+ v\sin 3\beta\lambda_5^R + \lambda_4 v\sin\beta + \lambda_4 v\sin 3\beta - 4\lambda_1 v\sin\beta\cos^2\beta + 4\lambda_3 v\sin\beta\cos^2\beta\Big] \\
&- 2\eta_3\lambda_5^I\left(\eta_2(3\sin 3\beta - \sin\beta) + 4v\cos 2\beta\right) - 2\eta_1^2\sin 2\beta\left(\lambda_1 - \lambda_3 - \lambda_4 + \lambda_5^R\right) \\
&+ 3\eta_3^2\left(4\lambda_2\sin\beta\cos^3\beta - 4\lambda_1\sin^3\beta\cos\beta - \sin 4\beta\left(\lambda_3 + \lambda_4 + \lambda_5^R\right)\right) \\
&+ 4\eta_2\cos\beta\Big[-\eta_2\lambda_4\sin\beta + \eta_2\sin\beta\lambda_5^R + v\cos 2\beta\lambda_5^R + v\lambda_5^R + \lambda_2\sin\beta\left(\eta_2 + 2v\sin\beta\right) \\
&- \lambda_3\sin\beta\left(\eta_2 + 2v\sin\beta\right) + \lambda_4 v\cos 2\beta - \lambda_4 v\Big]\Bigg) \\
&- \frac{T^2}{16v^2\cos\beta\sin\beta}\Big[8\left(\cos 2\beta\left(m_b^2 + m_t^2\right) - m_b^2 + m_t^2\right) + \lambda_1 v^2\sin^2 2\beta - \lambda_2 v^2\sin^2 2\beta\Big]
\end{aligned}
\tag{A.13}
$$

The temperature- and field-dependent masses $m_i^2(\eta_j, T)$ are obtained by diagonalizing this matrix.

A.2 Charged scalars

Debye corrections are added like for the neutral sector. We denote the two-by-two mass matrix of the charged sector by $\mathcal{P}^2_{ij}$. It is field- and temperature-dependent.

$$
\begin{aligned}
\mathcal{P}^2_{\mathrm{H}^+,\mathrm{H}^-} = \frac{1}{2}\sin^2\beta\tan\beta\Bigg(& \eta_1^2\cot\beta\left(\lambda_3\cot^2\beta + \lambda_1\right) \\
&+ 2\eta_1\cot\beta\Big[\cot\beta\left(\eta_3\cos\beta\lambda_5^I - \eta_2\lambda_5^R - v\sin\beta\lambda_5^R - \lambda_4\left(\eta_2 + v\sin\beta\right) + \lambda_3 v\cos\beta\cot\beta\right) \\
&+ \lambda_1 v\cos\beta\Big] + 2\eta_3\cot^2\beta\lambda_5^I\left(\eta_2\sin\beta + v\right) \\
&+ \eta_3^2\cos\beta\left(\lambda_1\sin\beta + \cos\beta\cot\beta\left(\lambda_2\cot^2\beta + 2\left(\lambda_3 + \lambda_4 + \lambda_5^R\right)\right)\right) \\
&+ \frac{1}{2}\cot\beta\csc^2\beta\Big[2\eta_2^2\left(\lambda_3\sin^2\beta + \lambda_2\cos^2\beta\right) + 4\mu^2 - 2v^2\lambda_5^R \\
&+ 2\eta_2 v\sin\beta\left(2\lambda_3\sin^2\beta + 2\lambda_2\cos^2\beta - 2\cos^2\beta\left(\lambda_4 + \lambda_5^R\right)\right) - 2\lambda_4 v^2\Big]\Bigg) \\
&+ \frac{T^2}{24}\Big[\left(6\lambda_1\sin^2\beta + 6\lambda_2\cos^2\beta + \frac{9}{2}g^2 + \frac{3}{2}g'^2 + 4\lambda_3 + 2\lambda_4\right) - 24\frac{m_b^2}{v^2}\tan^2\beta - 24\frac{m_t^2}{v^2}\cot^2\beta\Big]
\end{aligned}
\tag{A.14}
$$

$$
\begin{aligned}
\mathcal{P}^2_{\mathrm{H}^+,\mathrm{G}^-} = \frac{1}{16}\Bigg(& -4\eta_1^2\left(\lambda_1-\lambda_3\right)\sin 2\beta \\
& -4\eta_3^2\sin 2\beta\left(\lambda_1\sin^2\beta-\lambda_2\cos^2\beta+\lambda_3\cos 2\beta+\lambda_4\cos 2\beta+i\lambda_5^I+\cos 2\beta\lambda_5^R\right) \\
& -4\eta_1\Big[2i\eta_3\lambda_4\cos\beta-2\eta_2\lambda_4\cos 2\beta+\eta_3\cos\beta\lambda_5^I+\eta_3\cos 3\beta\lambda_5^I-2i\eta_2\lambda_5^I-2iv\sin\beta\lambda_5^I \\
& -2i\eta_3\cos\beta\lambda_5^R-2\eta_2\cos 2\beta\lambda_5^R+v\sin\beta\lambda_5^R-v\sin 3\beta\lambda_5^R+\lambda_4 v\sin\beta-\lambda_4 v\sin 3\beta \\
& +4\lambda_1 v\sin\beta\cos^2\beta-4\lambda_3 v\sin\beta\cos^2\beta\Big]-8\eta_3\left(\eta_2\sin\beta+v\right)\left(\cos 2\beta\lambda_5^I+i\lambda_4-i\lambda_5^R\right) \\
& +8\eta_2\cos\beta\left(v\left(\lambda_4\cos 2\beta+i\lambda_5^I+\cos 2\beta\lambda_5^R\right)+\lambda_2\sin\beta\left(\eta_2+2v\sin\beta\right)-\lambda_3\sin\beta\left(\eta_2+2v\sin\beta\right)\right)\Bigg) \\
& -\frac{T^2}{16v^2\cos\beta\sin\beta}\Big[8\left(\cos 2\beta\left(m_b^2+m_t^2\right)-m_b^2+m_t^2\right)+\lambda_1 v^2\sin^2 2\beta-\lambda_2 v^2\sin^2 2\beta\Big]
\end{aligned}
\tag{A.15}
$$

$$
\mathcal{P}^2_{\mathrm{G}^+,\mathrm{H}^-} = \left(\mathcal{P}^2_{\mathrm{H}^+,\mathrm{G}^-}\right)^* \tag{A.16}
$$

$$
\begin{aligned}
\mathcal{P}^2_{\mathrm{G}^+,\mathrm{G}^-} = \frac{1}{2}\sin^2\beta\Bigg(& \eta_1^2\left(\lambda_1\cot^2\beta+\lambda_3\right) \\
& +2\eta_1\cot\beta\left(\eta_2\lambda_4-\eta_3\cos\beta\lambda_5^I+\eta_2\lambda_5^R+v\sin\beta\lambda_5^R+\lambda_3 v\sin\beta+\lambda_4 v\sin\beta+\lambda_1 v\cos\beta\cot\beta\right) \\
& -2\eta_3\cot\beta\lambda_5^I\left(\eta_2\sin\beta+v\right) \\
& +\eta_3^2\left(\lambda_3\sin^2\beta+\lambda_1\cos^2\beta+\lambda_2\cos^2\beta-2\lambda_4\cos^2\beta+\lambda_3\cos^2\beta\cot^2\beta-2\cos^2\beta\lambda_5^R\right) \\
& +\eta_2\left(\cot^2\beta\left(2v\sin\beta\left(\lambda_4+\lambda_5^R\right)+\lambda_3\left(\eta_2+2v\sin\beta\right)\right)+\lambda_2\left(\eta_2+2v\sin\beta\right)\right)\Bigg) \\
& +\frac{T^2}{24}\left[6\lambda_2\sin^2\beta+6\lambda_1\cos^2\beta+\frac{9g^2}{2}+\frac{3g'^2}{2}+4\lambda_3+2\lambda_4-\frac{24m_b^2}{v^2}-\frac{24m_t^2}{v^2}\right]
\end{aligned}
\tag{A.17}
$$

A.3 Gauge bosons

For the gauge bosons we revert to the original gauge field basis and write the mass matrix

$$
\begin{aligned}
M^2(\phi,T) = M^2(\phi)+M_T^2(T) = & \\
& \begin{pmatrix} g^2\phi^2/4 & 0 & 0 & 0 \\ 0 & g^2\phi^2/4 & 0 & 0 \\ 0 & 0 & g^2\phi^2/4 & -gg'\phi^2/4 \\ 0 & 0 & -gg'\phi^2/4 & g'^2\phi^2/4 \end{pmatrix}+\begin{pmatrix} 2g^2T^2 & 0 & 0 & 0 \\ 0 & 2g^2T^2 & 0 & 0 \\ 0 & 0 & 2g^2T^2 & 0 \\ 0 & 0 & 0 & 2g'^2T^2 \end{pmatrix}\delta_T,
\end{aligned}
\tag{A.18}
$$

where $\phi = \eta_1 v\cos\beta+\eta_2 v\sin\beta+\frac{1}{2}\left(\eta_1^2+\eta_2^2+\eta_3^2+v^2\right)$ and the δ_T indicates that only transverse degrees of freedom get a temperature correction.

A.4 Fermions

Fermions do not get a thermal correction. The top quark gets it mass from Φ_2 and so does not depend on η_1. In a similar manner the bottom quark is granted its mass by Φ_1 and

does not depend on η_2.

$$M_t^2(\eta_j) = \frac{m_t^2\left(\eta_3^2\cot^2\beta + (\eta_2\csc\beta + v)^2\right)}{v^2} \tag{A.19}$$

$$M_b^2(\eta_j) = \frac{m_b^2\left(\eta_3^2\tan^2\beta + (\eta_1\sec\beta + v)^2\right)}{v^2} \tag{A.20}$$

References

[1] V. A. Kuzmin, V. A. Rubakov and M. E. Shaposhnikov, Phys. Lett. B **155** (1985) 36.

[2] V. A. Rubakov and M. E. Shaposhnikov, Usp. Fiz. Nauk **166** (1996) 493 [Phys. Usp. **39** (1996) 461] [hep-ph/9603208].

[3] D. E. Morrissey and M. J. Ramsey-Musolf, New J. Phys. **14** (2012) 125003 doi:10.1088/1367-2630/14/12/125003 [arXiv:1206.2942 [hep-ph]].

[4] K. Kajantie, M. Laine, K. Rummukainen and M. E. Shaposhnikov, Phys. Rev. Lett. **77** (1996) 2887 [hep-ph/9605288].

[5] M. B. Gavela, P. Hernandez, J. Orloff and O. Pene, Mod. Phys. Lett. A **9** (1994) 795 doi:10.1142/S0217732394000629 [hep-ph/9312215].

[6] M. B. Gavela, M. Lozano, J. Orloff and O. Pene, Nucl. Phys. B **430** (1994) 345 doi:10.1016/0550-3213(94)00409-9 [hep-ph/9406288].

[7] M. B. Gavela, P. Hernandez, J. Orloff, O. Pene and C. Quimbay, Nucl. Phys. B **430** (1994) 382 doi:10.1016/0550-3213(94)00410-2 [hep-ph/9406289].

[8] T. Brauner, O. Taanila, A. Tranberg and A. Vuorinen, Phys. Rev. Lett. **108** (2012) 041601 [arXiv:1110.6818 [hep-ph]].

[9] G. W. Anderson and L. J. Hall, Phys. Rev. D **45** (1992) 2685.

[10] D. Curtin, P. Meade and C. T. Yu, JHEP **1411** (2014) 127 [arXiv:1409.0005 [hep-ph]].

[11] P. H. Damgaard, A. Haarr, D. OConnell and A. Tranberg, JHEP **1602** (2016) 107 doi:10.1007/JHEP02(2016)107 [arXiv:1512.01963 [hep-ph]].

[12] P. H. Damgaard, D. O'Connell, T. C. Petersen and A. Tranberg, Phys. Rev. Lett. **111** (2013) 22, 221804 [arXiv:1305.4362 [hep-ph]].

[13] S. Profumo, M. J. Ramsey-Musolf and G. Shaughnessy, JHEP **0708** (2007) 010 [arXiv:0705.2425 [hep-ph]].

[14] J. M. Cline, K. Kainulainen and M. Trott, JHEP **1111** (2011) 089 [arXiv:1107.3559 [hep-ph]].

[15] L. Basso, P. Osland and G. M. Pruna, JHEP **1506** (2015) 083 doi:10.1007/JHEP06(2015)083 [arXiv:1504.07552 [hep-ph]].

[16] L. Basso, A. Lipniacka, F. Mahmoudi, S. Moretti, P. Osland, G. M. Pruna and M. Purmohammadi, PoS CHARGED **2012** (2012) 019 [arXiv:1301.4268 [hep-ph]].

[17] L. Basso, A. Lipniacka, F. Mahmoudi, S. Moretti, P. Osland, G. M. Pruna and M. Purmohammadi, JHEP **1211** (2012) 011 doi:10.1007/JHEP11(2012)011 [arXiv:1205.6569 [hep-ph]].

[18] A. W. El Kaffas, P. Osland and O. M. Ogreid, Nonlin. Phenom. Complex Syst. **10** (2007) 347 [hep-ph/0702097 [HEP-PH]].

[19] A. Wahab El Kaffas, P. Osland and O. M. Ogreid, Phys. Rev. D **76** (2007) 095001 doi:10.1103/PhysRevD.76.095001 [arXiv:0706.2997 [hep-ph]].

[20] A. W. El Kaffas, W. Khater, O. M. Ogreid and P. Osland, Nucl. Phys. B **775** (2007) 45 doi:10.1016/j.nuclphysb.2007.03.041 [hep-ph/0605142].

[21] W. Khater and P. Osland, Nucl. Phys. B **661** (2003) 209 doi:10.1016/S0550-3213(03)00300-6 [hep-ph/0302004].

[22] C. Y. Chen, S. Dawson and Y. Zhang, JHEP **1506** (2015) 056 doi:10.1007/JHEP06(2015)056 [arXiv:1503.01114 [hep-ph]].

[23] S. Inoue, M. J. Ramsey-Musolf and Y. Zhang, Phys. Rev. D **89** (2014) no.11, 115023 doi:10.1103/PhysRevD.89.115023 [arXiv:1403.4257 [hep-ph]].

[24] G. C. Dorsch, S. J. Huber and J. M. No, JHEP **1310** (2013) 029 doi:10.1007/JHEP10(2013)029 [arXiv:1305.6610 [hep-ph]].

[25] G. C. Dorsch, S. J. Huber, K. Mimasu and J. M. No, Phys. Rev. Lett. **113** (2014) no.21, 211802 doi:10.1103/PhysRevLett.113.211802 [arXiv:1405.5537 [hep-ph]].

[26] L. Fromme, S. J. Huber and M. Seniuch, JHEP **0611** (2006) 038 doi:10.1088/1126-6708/2006/11/038 [hep-ph/0605242].

[27] J. M. Cline and P. A. Lemieux, Phys. Rev. D **55** (1997) 3873 [hep-ph/9609240].

[28] P. B. Arnold and O. Espinosa, Phys. Rev. D **47** (1993) 3546 [Erratum-ibid. D **50** (1994) 6662] [hep-ph/9212235].

[29] N. Blinov, S. Profumo and T. Stefaniak, JCAP **1507** (2015) no.07, 028 doi:10.1088/1475-7516/2015/07/028 [arXiv:1504.05949 [hep-ph]].

[30] G. C. Branco, P. M. Ferreira, L. Lavoura, M. N. Rebelo, M. Sher and J. P. Silva, Phys. Rept. **516** (2012) 1 doi:10.1016/j.physrep.2012.02.002 [arXiv:1106.0034 [hep-ph]].

[31] I. F. Ginzburg and M. Krawczyk, Phys. Rev. D **72** (2005) 115013 doi:10.1103/PhysRevD.72.115013 [hep-ph/0408011].

[32] B. Grzadkowski, O. M. Ogreid and P. Osland, JHEP **1411** (2014) 084 doi:10.1007/JHEP11(2014)084 [arXiv:1409.7265 [hep-ph]].

[33] B. Grzadkowski, O. M. Ogreid and P. Osland, JHEP **1401** (2014) 105 doi:10.1007/JHEP01(2014)105 [arXiv:1309.6229 [hep-ph]].

[34] F. Staub, Adv. High Energy Phys. **2015** (2015) 840780 doi:10.1155/2015/840780 [arXiv:1503.04200 [hep-ph]].

[35] W. Porod, Comput. Phys. Commun. **153** (2003) 275 doi:10.1016/S0010-4655(03)00222-4 [hep-ph/0301101].

[36] W. Porod and F. Staub, Comput. Phys. Commun. **183** (2012) 2458 doi:10.1016/j.cpc.2012.05.021 [arXiv:1104.1573 [hep-ph]].

[37] R. R. Parwani, Phys. Rev. D **45** (1992) 4695 Erratum: [Phys. Rev. D **48** (1993) 5965] doi:10.1103/PhysRevD.45.4695, 10.1103/PhysRevD.48.5965.2 [hep-ph/9204216].

[38] M. E. Carrington, Phys. Rev. D **45** (1992) 2933. doi:10.1103/PhysRevD.45.2933

[39] J. E. Camargo-Molina, B. O'Leary, W. Porod and F. Staub, Eur. Phys. J. C **73** (2013) no.10, 2588 doi:10.1140/epjc/s10052-013-2588-2 [arXiv:1307.1477 [hep-ph]].

[40] L. Dolan and R. Jackiw, Phys. Rev. D **9** (1974) 3320. doi:10.1103/PhysRevD.9.3320

[41] M. Garny and T. Konstandin, JHEP **1207** (2012) 189 doi:10.1007/JHEP07(2012)189 [arXiv:1205.3392 [hep-ph]].

[42] C. Wainwright, S. Profumo and M. J. Ramsey-Musolf, Phys. Rev. D **84** (2011) 023521 doi:10.1103/PhysRevD.84.023521 [arXiv:1104.5487 [hep-ph]].

[43] H. H. Patel and M. J. Ramsey-Musolf, JHEP **1107** (2011) 029 doi:10.1007/JHEP07(2011)029 [arXiv:1101.4665 [hep-ph]].

[44] M. D'Onofrio, K. Rummukainen and A. Tranberg, JHEP **1208** (2012) 123 [arXiv:1207.0685 [hep-ph]].

[45] F. Feroz and M. P. Hobson, Mon. Not. Roy. Astron. Soc. **384** (2008) 449 doi:10.1111/j.1365-2966.2007.12353.x [arXiv:0704.3704 [astro-ph]].

[46] F. Feroz, M. P. Hobson and M. Bridges, Mon. Not. Roy. Astron. Soc. **398** (2009) 1601 doi:10.1111/j.1365-2966.2009.14548.x [arXiv:0809.3437 [astro-ph]].

[47] F. Feroz, M. P. Hobson, E. Cameron and A. N. Pettitt, arXiv:1306.2144 [astro-ph.IM].

[48] J. Buchner *et al.*, Astron. Astrophys. **564** (2014) A125 doi:10.1051/0004-6361/201322971 [arXiv:1402.0004 [astro-ph.HE]].

[49] Skilling J., 2004, AIP Conference Proceedings of the 24th International Workshop on Bayesian Inference and Maximum Entropy Methods in Science and Engineering, Vol. 735, pp. 395-405

[50] P. Bechtle, O. Brein, S. Heinemeyer, G. Weiglein and K. E. Williams, Comput. Phys. Commun. **181** (2010) 138 doi:10.1016/j.cpc.2009.09.003 [arXiv:0811.4169 [hep-ph]].

[51] P. Bechtle, O. Brein, S. Heinemeyer, G. Weiglein and K. E. Williams, Comput. Phys. Commun. **182** (2011) 2605 doi:10.1016/j.cpc.2011.07.015 [arXiv:1102.1898 [hep-ph]].

[52] P. Bechtle, O. Brein, S. Heinemeyer, O. Stal, T. Stefaniak, G. Weiglein and K. Williams, PoS CHARGED **2012** (2012) 024 [arXiv:1301.2345 [hep-ph]].

[53] P. Bechtle, O. Brein, S. Heinemeyer, O. Stl, T. Stefaniak, G. Weiglein and K. E. Williams, Eur. Phys. J. C **74** (2014) no.3, 2693 doi:10.1140/epjc/s10052-013-2693-2 [arXiv:1311.0055 [hep-ph]].

[54] P. Bechtle, S. Heinemeyer, O. Stal, T. Stefaniak and G. Weiglein, Eur. Phys. J. C **75** (2015) no.9, 421 doi:10.1140/epjc/s10052-015-3650-z [arXiv:1507.06706 [hep-ph]].

[55] P. Bechtle, S. Heinemeyer, O. Stl, T. Stefaniak and G. Weiglein, Eur. Phys. J. C **74** (2014) no.2, 2711 doi:10.1140/epjc/s10052-013-2711-4 [arXiv:1305.1933 [hep-ph]].

[56] O. Stl and T. Stefaniak, PoS EPS **-HEP2013** (2013) 314 [arXiv:1310.4039 [hep-ph]].

[57] P. Bechtle, S. Heinemeyer, O. Stl, T. Stefaniak and G. Weiglein, JHEP **1411** (2014) 039 doi:10.1007/JHEP11(2014)039 [arXiv:1403.1582 [hep-ph]].

[58] G. Aad *et al.* [ATLAS and CMS Collaborations], JHEP **1608** (2016) 045 doi:10.1007/JHEP08(2016)045 [arXiv:1606.02266 [hep-ex]].

[59] ATLAS Collaboration, ATLAS-CONF-2016-067

[60] ATLAS Collaboration, ATLAS-CONF-2016-079

[61] CMS Collaboration, CMS-PAS-HIG-16-020

[62] CMS Collaboration, CMS-PAS-HIG-16-033

[63] I. F. Ginzburg and I. P. Ivanov, Phys. Rev. D **72** (2005) 115010 doi:10.1103/PhysRevD.72.115010 [hep-ph/0508020].

[64] B. Grinstein, C. W. Murphy and P. Uttayarat, JHEP **1606** (2016) 070 doi:10.1007/JHEP06(2016)070 [arXiv:1512.04567 [hep-ph]].

[65] V. Cacchio, D. Chowdhury, O. Eberhardt and C. W. Murphy, arXiv:1609.01290 [hep-ph].

[66] R. Ruiz de Austri, R. Trotta and L. Roszkowski, JHEP **0605** (2006) 002 doi:10.1088/1126-6708/2006/05/002 [hep-ph/0602028].

[67] K. A. Olive *et al.* [Particle Data Group Collaboration], Chin. Phys. C **38** (2014) 090001. doi:10.1088/1674-1137/38/9/090001

[68] Y. Amhis *et al.* [Heavy Flavor Averaging Group (HFAG) Collaboration], arXiv:1412.7515 [hep-ex].

[69] A. G. Akeroyd and S. Recksiegel, J. Phys. G **29** (2003) 2311 doi:10.1088/0954-3899/29/10/301 [hep-ph/0306037].

[70] A. G. Akeroyd and C. H. Chen, Phys. Rev. D **75** (2007) 075004 doi:10.1103/PhysRevD.75.075004 [hep-ph/0701078].

[71] F. Mahmoudi, Comput. Phys. Commun. **178** (2008) 745 doi:10.1016/j.cpc.2007.12.006 [arXiv:0710.2067 [hep-ph]].

[72] F. Mahmoudi, Comput. Phys. Commun. **180** (2009) 1579 doi:10.1016/j.cpc.2009.02.017 [arXiv:0808.3144 [hep-ph]].

[73] M. Misiak *et al.*, Phys. Rev. Lett. **114** (2015) no.22, 221801 doi:10.1103/PhysRevLett.114.221801 [arXiv:1503.01789 [hep-ph]].

[74] T. Enomoto and R. Watanabe, JHEP **1605** (2016) 002 doi:10.1007/JHEP05(2016)002 [arXiv:1511.05066 [hep-ph]].

[75] F. James and M. Roos, Comput. Phys. Commun. **10** (1975) 343. doi:10.1016/0010-4655(75)90039-9

[76] P. M. Ferreira, J. F. Gunion, H. E. Haber and R. Santos, Phys. Rev. D **89** (2014) no.11, 115003 doi:10.1103/PhysRevD.89.115003 [arXiv:1403.4736 [hep-ph]].

[77] B. Dumont, J. F. Gunion, Y. Jiang and S. Kraml, Phys. Rev. D **90** (2014) 035021 doi:10.1103/PhysRevD.90.035021 [arXiv:1405.3584 [hep-ph]].

[78] R. E. Kass and A. E. Raftery, JASA **90** (1995) 430.

[79] S. Chang, S. K. Kang, J. P. Lee and J. Song, Phys. Rev. D **92** (2015) no.7, 075023 doi:10.1103/PhysRevD.92.075023 [arXiv:1507.03618 [hep-ph]].

[80] I. P. Ivanov and J. P. Silva, Phys. Rev. D **92** (2015) no.5, 055017 doi:10.1103/PhysRevD.92.055017 [arXiv:1507.05100 [hep-ph]].

[81] J. Bernon, J. F. Gunion, Y. Jiang and S. Kraml, Phys. Rev. D **91** (2015) no.7, 075019 doi:10.1103/PhysRevD.91.075019 [arXiv:1412.3385 [hep-ph]].

[82] D. Chowdhury and O. Eberhardt, JHEP **1511** (2015) 052 doi:10.1007/JHEP11(2015)052 [arXiv:1503.08216 [hep-ph]].

[83] A. Buckley, Eur. Phys. J. C **75** (2015) no.10, 467 doi:10.1140/epjc/s10052-015-3638-8 [arXiv:1305.4194 [hep-ph]].

[84] P. Scott, Eur. Phys. J. Plus **127** (2012) 138 doi:10.1140/epjp/i2012-12138-3 [arXiv:1206.2245 [physics.data-an]].